

1 **Integrating field, textural and geochemical monitoring to track eruption triggers and**
2 **dynamics: a case-study from Piton de la Fournaise**

3

4 Lucia Gurioli⁽¹⁾, Andrea Di Muro⁽²⁾, Ivan Vlastélic⁽¹⁾, Séverine Moune⁽¹⁾, Simon Thivet⁽¹⁾,
5 Marina Valer⁽¹⁾, Nicolas Villeneuve⁽²⁾, Guillaume Boudoire^(2,3), Aline Peltier⁽²⁾, Patrick
6 Bachèlery⁽¹⁾, Valerie Ferrazzini⁽²⁾, Nicole Métrich⁽²⁾, Mhammed Benbakkar⁽¹⁾, Nicolas
7 Cluzel⁽¹⁾, Christophe Constantin⁽¹⁾, Jean-Luc Devidal⁽¹⁾, Claire Fonquernie⁽¹⁾, Jean-Marc
8 Hénot⁽¹⁾

9 (1) Université Clermont Auvergne, CNRS, IRD, OPGC, Laboratoire Magmas et Volcans, F-63000
10 Clermont-Ferrand, France

11 (2) Institut de Physique du Globe (IPGP), Sorbonne Paris-Cite, CNRS UMR-7154, Université Paris
12 Diderot, Observatoire Volcanologique du Piton de la Fournaise (OVPF), Bourg Murat, France,

13 (3) Laboratoire Géosciences Réunion, Université de La Réunion, Institut de Physique du Globe de
14 Paris, Sorbonne Paris-Cité, UMR 7154 CNRS, F-97715 Saint-Denis, France

15 Corresponding author: L Gurioli, Université Clermont Auvergne, CNRS, IRD, OPGC, LMV
16 Campus Universitaire des Cézeaux, 6 Avenue Blaise Pascal, 63178 Aubière Cedex
17 (lucia.gurioli@uca.fr)

18

19 **Abstract**

20 The 2014 eruption at Piton de la Fournaise (PdF), La Réunion, which occurred after 41
21 months of quiescence, began with surprisingly little precursory activity, and was one of the
22 smallest so far observed at PdF in terms of duration (less than 2 days) and volume (less than
23 $0.4 \times 10^6 \text{ m}^3$). The pyroclastic material was composed of golden basaltic pumice along with
24 fluidal, spiny-iridescent and spiny-opaque, ~~spiny iridescent, and fluidal~~ basaltic scoria ~~along~~
25 ~~with golden basaltic pumice~~. Density analyses performed on 200 lapilli reveal that the spiny-
26 opaque clasts are the densest (1600 kg/m^3) and richest in crystals (55 vol. %), and the golden
27 pumices are the lightest-least dense (400 kg/m^3) and poorest in crystals (8 vol. %). The
28 connectivity data indicate that the fluidal and golden (Hawaiian-like) clasts have more
29 isolated vesicles (up to 40 vol. %) than the spiny (Strombolian-like) clasts (0-5 vol. %). These
30 textural variations are linked to primary pre-eruptive magma storage conditions. The golden
31 and fluidal fragments track the hotter portion of the melt, in contrast to the spiny fragments
32 and lava that mirror the cooler portion of the shallow reservoir. Exponential decrease of the

33 magma ascent and output rates corresponded to progressive tapping of these distinct portions
34 of the storage system. Increasing syn-eruptive degassing and melt-gas decoupling lead to a
35 decrease in the explosive intensity from early fountaining to Strombolian activity. The
36 geochemical results confirm the absence of new hot input of magma into the 2014 reservoir
37 and confirm the emission of a single, shallow, differentiated magma source, possibly related
38 to residual magma from the November 2009 eruption. Fast volatile exsolution and crystal-
39 melt separation (second boiling) were triggered by deep pre-eruptive magma transfer and
40 stress field change. Our study highlights the possibility that shallow magma pockets can be
41 quickly reactivated by deep processes without mass or energy (heat) transfer and produce
42 hazardous eruptions with only short term elusive precursors.

43 **Key words:** Piton de la Fournaise, Hawaiian activity, Strombolian activity, shallow reservoir,
44 texture, petrology, geochemistry

45 1. Introduction

46 A detailed characterization and understanding of eruptive dynamics and of processes driving
47 and modulating volcano unrest is crucial in monitoring active volcanoes and fundamental for
48 forecasting volcanic eruptions (Sparks, 2003). Many studies suggest that eruptive phenomena
49 are strongly dependent on the physico-chemical properties of ascending magma in the conduit
50 (e.g., temperature, viscosity, porosity, and permeability) (e.g. Sparks, 1978; Rust and
51 Cashman, 2011; Gonnermann and Manga, 2013; Polacci et al., 2014). Integrating
52 petrographic, chemical and textural data can thus provide critical information to constrain
53 both the pre-eruptive storage conditions, and the processes related to magma ascent, degassing
54 and cooling (e.g., reference in Table 1 in Gurioli et al., 2015). This multidisciplinary approach
55 is of even greater importance in the monitoring of volcanoes which emit relatively uniform
56 magma compositions over time, like basaltic volcanoes (e.g. Di Muro et al., 2014; Gurioli et
57 al., 2015; Coppola et al., 2017). As a result, monitoring of textures, and petrochemical
58 properties of lava fragments and pyroclasts is now routinely carried out on a daily basis at
59 active volcanoes such as Kilauea, Etna, and Stromboli (e.g., [Taddeucci et al., 2002](#); Thornber
60 et al., 2003; Polacci et al., 2006; Swanson et al., 2009; ~~Taddeucci et al., 2002~~; Colo' et al.,
61 2010; Houghton et al., 2011; 2013; 2016; Carey et al., 2012; 2013; Lautze et al., 2012;
62 Andronico et al., 2013a; b; 2014; ~~Corsaro and and Miraglia, 2014~~; Di Muro et al., 2014;
63 [Gurioli et al.; 2014](#); Eychenne et al., 2015; ~~Gurioli et al.; 2014~~; Leduc et al., 2015; Kahl et al.,
64 2015). In the past, time series of petrographic and geochemical data have been measured for

65 ~~Piton de la Fournaise P~~(PdF) basalts and particularly for effusive products. The aim of these
66 datasets was to constrain ~~time and space~~the spatial and temporal evolution of magma
67 ~~evolution~~ for one of the most active basaltic volcanoes of the world (e.g. Albarède et al., 1997;
68 Vlastélic et al., 2005; 2007, 2009; Boivin and Bachèlery, 2009; Peltier et al., 2009; Schiano et
69 al., 2012; Vlastèlic and Pietruszka, 2016; Schiano et al., 2012; Boivin and Bachèlery, 2009;
70 Peltier et al., 2009; Lénat et al., 2012; Di Muro et al., 2014; 2015; Vlastèlic and Pietruszka,
71 2016). However, this type of approach has seldom been coupled with detailed textural studies
72 at PdF and instead has mostly focused on crystal textures and crystal size distribution (Welsch
73 et al., 2009; 2013; Di Muro et al., 2014; 2015). Moreover, only sporadic data exist on the
74 textures of pyroclasts ejected by the eruptions at PdF (Villemant et al., 2009; Famin et al.,
75 2009; Welsch et al., 2009; 2013; Michon et al., 2013; Vlastélic et al., 2013; ~~Welsch et al.,~~
76 ~~2009; 2013;~~ Di Muro et al., 2015; Morandi et al., 2016; ~~Di Muro et al., 2015;~~ Ort et al., 2016).

77 Within this paper, we present a multidisciplinary textural, chemical and petrological
78 approach to quantify and understand the short-lived 2014 PdF eruption. This approach
79 combines detailed study of the pyroclastic deposit (grain size and componentry) with bulk
80 texture analysis (density, vesicularity, connectivity, permeability, morphology, vesicle
81 distribution and crystal content) and a petro-chemical study (bulk rock, glass, minerals, melt
82 inclusions) of the same clasts. This integrated approach has now been formalized within the
83 French National Observation Service for Volcanology (SNOV), as routine observational
84 systems (DynVolc), Dynamics of Volcanoes, ([http://wwwobs.univ-](http://wwwobs.univ-bpclermont.fr/SO/televolc/dynvolc/)
85 [bpclermont.fr/SO/televolc/dynvolc/](http://wwwobs.univ-bpclermont.fr/SO/televolc/dynvolc/)) and GazVolc, Observation des gaz volcaniques,
86 (<http://wwwobs.univ-bpclermont.fr/SO/televolc/gazvolc/>) to provide data for the on-going
87 activity at PdF (Harris et al., 2017).

88 In spite of being the first of a series of eruptions, the June 2014 event was preceded by
89 only weak inflation and by a rapid increase in number of shallow (< 2 km below volcano
90 summit) volcano tectonic earthquakes that happened only 11 days before the eruption (Peltier
91 et al., 2016). The eruptive event was dominantly effusive, lasted only 20 hours and emitted a
92 very small volume of magma (ca. $0.4 \times 10^6 \text{ m}^3$, Peltier et al., 2016), which makes this event
93 one of the smallest, in terms of duration and volume, observed at PdF up to now. In addition,
94 the eruption started during the night and very little direct observation exists for the first few
95 hours of the activity, when the lava effusion was associated with very weak fountaining
96 activity and Strombolian explosions.

97 This eruption occurred just outside the southern border of the summit Dolomieu
98 caldera, at the top of the central cone of PdF (Fig. 1). This is a high risk sector because of the

99 high number of tourists. Identification of precursors of this kind of activity represents an
100 important challenge for monitoring systems (Bachelery et al., 2016).

101 Therefore this eruption represents an ideal context to apply our multidisciplinary
102 approach, with the aim of addressing the following key questions:

103 (i) why was such a small volume of magma erupted instead of remaining
104 ~~intruded~~ endogenic?

105 (ii) what caused the rapid trigger and the sudden end to this small volume
106 eruption?

107 (iii) which was the source of the eruption (shallow versus deep, single versus
108 multiple small magma batches)?

109 (iv) what was the ascent and degassing history of the magma?

110 (v) what was the time and space evolution of the eruptive event?

111 Furthermore, this eruption provides an exceptional opportunity to study processes leading to
112 the transition from mild Hawaiian (<20 m high fountains, following the nomenclature
113 proposed by Stovall et al., 2011) to Strombolian activity (<10 m high explosions), whose
114 products are little modified by post-fragmentation processes because of the very low intensity
115 of the activity.

116 **2 The 2014 activity**

117 **2.1 Precursory activity**

118 The 20 June 2014 summit eruption represents the first eruption at PdF after 41 months of
119 quiescence. The last eruption had been on 9 December 2010, with a shallow (above sea level)
120 intrusion on 2 February 2011 (Roult et al., 2012). From 2011, the deformation at PdF was
121 constant with two distinct types of behaviour: (i) a summit contraction of a few centimetres
122 every year (Fig. 1d); and (ii) a preferential displacement of the east flank at a rate of 1-3
123 centimetres per year (Brenquier et al., 2012; Staudacher and Peltier, 2015). The background
124 microseismicity was very low (< 5 shallow events/day below volcano summit) and low-
125 temperature summit intracaldera fumaroles emitted very little sulphur (H₂S or SO₂) and
126 carbon (CO₂) (Di Muro et al., 2016). After 41 months of rest, a new intense cycle of activity
127 (June 2014, February 2015, May 2015, July 2015, August-October 2015; May 2016;
128 September 2016; January 2017 and July 2017) began with surprisingly little and ambiguous
129 precursory activity.

130 The 2014 summit eruption started during the night of June 20/21, at 21h35 GMT
131 (0h35 local time) and ended on June 21 at 17h09 GMT (21h09 local time), after less than 20
132 hours of dominantly effusive activity. The volcano reawakening was preceded, in March and
133 April 2014, by deep (15-20 km below sea level) eccentric seismicity and increase in soil CO₂
134 flux below the western volcano flank, 15 km NW of the volcano summit (Liuzzo et al., 2015;
135 Boudoire et al., 2017). Background micro-seismicity and inflation of the central cone
136 increased progressively starting on 9 June 2014. Weak inflation recorded on both distal and
137 summit baselines (Fig. 1d) suggest that deep (below sea level) magma up-rise was
138 pressurizing the shallow (above sea level) magma storage system (Peltier et al., 2016). On
139 June 13, 17 and 20, three shallow (hypocentres located above sea level) intense seismic crises
140 occurred below the summit Dolomieu caldera (Fig. 1), with hundreds of events located in a
141 narrow depth range between 1100 and 2100 metres below the volcano summit. These seismic
142 crises consisted of swarms of low magnitude (M: 1-2) volcano tectonic events which
143 increased in number from the first to the third crisis. On June 20, seismicity increased
144 progressively and a final seismic crisis started at 20h20 GMT, only 75 minutes before the
145 eruption. This last seismic crisis was coupled with acceleration in the deformation of the
146 summit area, which began only 60 minutes before the eruption. Interestingly, only slight
147 inflation of the central cone (< 2 cm of dilatation) was detected 11 days before the 2014
148 eruption with a maximum of 1 cm and 1.6 cm enlargement at the summit and the base of the
149 cone, respectively (Peltier et al., 2016 and Fig. 1d). A moderate increase in CO₂ and H₂S
150 emissions from summit intracaldera fumaroles was detected starting on June 2, but only very
151 minor SO₂ emissions occurred before the eruption (mostly on June 7 and 15, unpublished
152 data). Therefore, the acceleration in both geophysical and geochemical parameters was mostly
153 related to the late phase of dyke propagation towards the surface just before the eruption.
154 Following the end of the June 20-21 eruption, a long-term continuous inflation of the edifice
155 began, at a moderate rate, and mostly at the base of the volcano. More than one year after this
156 first eruption, the long-term deformation trends showed that the 2014 eruption marked a kink
157 between the deflation trend which followed the caldera-forming 2007 eruption (Staudacher et
158 al., 2009) and the currently ongoing continuous inflation trend (Fig. 1d, and Peltier et al.,
159 2016; Coppola et al., 2017).

160 2.2 Chronology of the events

161 We reconstructed the chronology of [the](#) events by combining a distribution map of the
162 fissures, pyroclastic deposits and lava flows (Fig. 1) with a review of available images (~~visible~~

163 | ~~and IR~~) and videos extracted from the observatory data base, the local newspapers, and web
164 sites (Fig. 2). The 2014 eruption occurred at the summit and on the SE slopes of the Dolomieu
165 Caldera (Figs. 1a, 1b and 1c) and evolved quickly and continuously over 20 hours. The full
166 set of fractures opened during a short period of time (minutes) and emitted short (<1.7 km
167 long) lava flows (Fig. 1 and Figs. 2c and 2d). Feeding vents were scattered along a 0.6 km
168 long fissure set (Fig. 1a) and produced very weak (low) Hawaiian to Strombolian activity
169 (Fig. 2).

170 Fissures opened from west to east, initially sub-parallel to the southern border of
171 Dolomieu caldera and then propagated at lower altitude (Fig. 1). The summit part of the
172 fractures (ca. 2500 m asl, Western Fracture, WF in Fig. 1) emitted only small volumes of lava
173 and pyroclasts. This part of the fracture set was active only during the first few hours of the
174 eruption, at night. The eastern part of the fractures (Upper Fracture, UF in Fig. 1) descended
175 to lower altitude (between 2400 and 2300 m asl, Middle Fracture, Fig. 1) along the SE flank
176 of the summit cone and emitted most of the erupted volume. As often observed in PdF
177 eruptions, the activity progressively focused on a narrow portion of the fractures at low
178 altitude and finally on a single vent located at the lower tip of the fracture system (Main Vent,
179 at 2336 m asl, MV in Figs. 1, 2). The first in situ observations in the morning of June 21 (ca.
180 04h00 GMT) showed that weak Strombolian activity (Figs. 2a and 2b) was focused on a
181 narrow segment of the lower fractures and that a'a lavas had already attained the elevation of
182 1983 m asl (0.2 km before maximum runout, Fig. 2c). A small, weak gas plume was also
183 blowing northwards. A single sample of partially molten lava was collected from the still
184 | active lava front and partially water quenched (REUeu140621-1, Table S1, Fig. 2d). During
185 most of June 21, the activity consisted of lava effusion in three parallel lava streams (Fig. 2c)
186 merging in a single lava flow (Fig. 2e) and mild-weak "Strombolian" explosions at several
187 closely spaced spots along the lower part of the feeding fracture. At 13.00 (GMT), only weak
188 explosions were observed within a single small spatter cone (Figs. 2f and 2g). Most of the
189 lava field was formed of open channel a'a lavas. The total volume of lava was estimated by
190 MIROVA service (<https://www.sites.google.com/site/mirovaweb/home>), with the use of the
191 MODIS images and the analyses of the flux from the spectral properties, to be within $0.34 \pm$
192 $0.12 \times 10^6 \text{ m}^3$, (Coppola et al., 2017). Satellite derived volume estimates are consistent with
193 independent photogrammetric estimates ($0.4 \pm 0.2 \times 10^6 \text{ m}^3$; Peltier et al., 2016) and rank the
194 2014 eruption at the lower end of the volume range typically emitted by PdF (Roult et al.,
195 2012).

196 3. Methodology

197 3.1 Sampling strategy

198 Apart from the sample from the front of the still active lava flow (Fig. 2d), all other samples
199 were collected in two phases: 3 days ~~after the eruption~~ (pyroclasts on June 24, Fig. 3a and
200 Table S1) and 11 days ~~after the eruption~~ (lavas on July 2, Table S1), and three months later
201 (pyroclasts from the MV, Fig. 1, on November 18 and ~~Table S1~~). June 24 samples were
202 collected both from the main fractures (WF and UF, Fig. 1a), the MV and the active lava flow
203 (Fig. 1 and Table S1). Twenty five scoriaceous bombs and lapilli (REU140624-9a-1 to
204 REU140624-9a and REU140624-9b-6 to REU140624-9b-25, in Table S3) were collected
205 from the discontinuous deposit (Fig. 3d) emplaced at the WF site (Fig. 1a), active only at the
206 beginning of the eruptive event. Because of the short duration of the activity at the WF, the
207 scoria fragments on the ground were scarce (Fig. 3de). The strategy was to collect a sample
208 that was formed by the largest available number of clasts that was representative of this
209 discrete deposit (REU140624-9 in Table S1). From the ~~Upper Fracture~~ (UF ~~in~~ Fig. 1a) only
210 one big scoria was collected (REU140624-13, Table S1) that broke in five parts, allowing us
211 to measure its vesiculated core and the dense quenched external part (REU140624-13-a to
212 REU140624-13-e, in Table S3). In contrast, the sustained and slightly more energetic activity
213 at the lower tip of the fractures, at the MV site, built a small spatter cone (Fig. 2) and
214 accumulated a continuous, small volume ~~continuous~~ deposit (Fig. 3a) of inversely graded
215 scoria fallout (Figs. 3b and 3c). This deposit is 10 cm thick at 2 m from the vent and covers an
216 area of about $\sim 1000 \text{ m}^2$ ~~(Main Vent, MV, Fig. 1)~~. For this fall deposit we collected two bulk
217 samples, one from the base (within the lower 5 cm, REU141118-6 in Table S1) and the other
218 from the top (within the upper 5 cm, REU140624-3, in Table S1), for the grain size (Fig. 3c)
219 and componentry analyses. The sample at the base was collected in November because on
220 June 24 the loose proximal lapilli blanket was still very hot (405 °C; thermocouple
221 measurement, ~~Fig. 3a~~) and fumaroles with outlet temperatures in the range 305-60 °C were
222 sampled all along the fractures several weeks after the eruption (Fig. 1b and Table S1). These
223 latter geochemical data are not presented in this paper. We selected 103 fragments from the
224 coarse grained bulk deposit within the upper 5 cm at the top of the scoria fall out deposit (Fig.
225 3b) at MV (REU140624-3-1 to REU140624-3-103, in Table S3) for density, connectivity,
226 permeability, petrological and geochemical analysis. In addition, in November 2014, more
227 than 200 clasts (comprising the REU141118-1 to REU141118-5 samples, Table S1) of similar
228 size (maximum diameter between 16 and 32 mm, see Gurioli et al., 2015) were collected, both

229 | close to the MV and in the ‘distal’ area (30 metres away from the MV sitet) to complete the
230 | particle bulk texture analyses and the chemical analyses.

231 | **3.2 Grain size and componentry**

232 | We performed grain size analyses on the two bulk samples collected from the MV, following
233 | the procedure of Jordan et al. (2015) (Table S2). The samples were dried in the oven at 90°C
234 | and sieved at $\frac{1}{2}$ phi intervals in the range of -5ϕ to 4ϕ (Fig. 3c); the data are also shown in
235 | full phi for comparison with the deposits of the 2010 PdF fountaining episode (Hibert et al.,
236 | 2015; Fig. 3f). Sieving was carried out by hand and for not longer than three minutes to avoid
237 | breaking and abrasion of the very vesicular and fragile clasts. For the scattered scoria sampled
238 | from the WF (Figs. 1, 3d and 3e), we followed the grain size strategy proposed in Gurioli et
239 | al. (2013). Within this procedure we sampled each fragment and we recorded the weight and
240 | the three main axes (a being the largest, b, and c). To allow comparison with the sieving grain
241 | size analyses (Inman, 1952), we used the intermediate b axis dimension to obtain $\phi = -\log_2 b$.

242 | Following the nomenclature of White and Houghton (2006) the componentry analysis
243 | is the subdivision of the sample into three broad components: i) juvenile, ii) non-juvenile
244 | particles, and iii) composite clasts. The juvenile components are vesicular or dense fragments,
245 | as well as crystals, that represent the primary magma involved in the eruption; non-juvenile
246 | material includes accessory and accidental fragments, as well as crystals that predate the
247 | eruption from which they are deposited. Finally, the composite clasts are mechanical mixtures
248 | of juvenile and non-juvenile (and/or recycled juvenile) clasts. In these mild basaltic
249 | explosions, the non-juvenile component is very scarce, so we focused on the juvenile
250 | component that is characterized by three groups of scoria: (i) spiny-opaque, (ii) spiny-glassy,
251 | and (iii) fluidal, along with golden pumice (Fig. 4). The componentry quantification was
252 | performed for each grain size fraction between -5ϕ to 0.5ϕ (Figs. 5a and 5b), where a
253 | binocular microscope was used for the identification of grains smaller than -1ϕ (Table S2).

254 | In the following, we will use the crystal nomenclature of Welch et al. (2009), with the
255 | strictly descriptive terms of macrocrysts (> 3 mm in diameter) mesocrysts (from 0.3 to 3 mm
256 | in diameter), and microcrysts (< 0.3 mm in diameter). ~~Regarding the June 2014 products,~~
257 | ~~these ranges of size may however change in comparison to the December 2005 products~~
258 | ~~studied by Welsch et al. (2009).~~ Regarding the June 2014 products, these ranges of size may
259 | however change in comparison to the December 2005 products studied by Welsch et al.
260 | (2009).

261 3.3 Particle bulk texture (density, porosity, connectivity, permeability) and microtexture

262 For each sample site (WF, UF and MV, Fig. 1a), we selected all the available particles within
263 the 8-32 mm fraction for density/porosity, connectivity and permeability measurements (Table
264 S3). This is the smallest granulometric fraction assumed to be still representative of the larger
265 size class in terms of density (Houghton and Wilson, 1989; Gurioli et al., 2015), and has been
266 used in previous textural studies (e.g., Shea et al., 2010). In addition, this size range is ideal
267 for vesicle connectivity measurements (e.g. Formenti and Druitt, 2003; Giachetti et al., 2010;
268 Shea et al., 2012; Colombier et al., 2017a, b). Density of juvenile particles was measured by
269 the water-immersion technique of Houghton and Wilson (1989), which is based on
270 Archimedes principle. A mean value for the vesicle-free rock density was determined by
271 powdering clasts of varying bulk densities, measuring the volumes of known masses using an
272 Accupyc 1340 Helium Pycnometer, then averaging. The same pycnometer was also used to
273 measure vesicle interconnectivity for each clast using the method of Formenti and Druitt
274 (2003) and Colombier et al. (2017a). Permeability measurements were performed on five
275 clasts: two golden pumices, one fluidal, one spiny glassy and one opaque scoria, all collected
276 from the MV (Table S3). Following Colombier et al. (2017a), the clasts were cut into
277 rectangular prisms to enable precise calculation of the cross-sectional area, which is required
278 to calculate permeability. These prisms were then embedded in a viscous resin, which was left
279 to harden for 24 h. The sample surface had been previously coated with a more viscous resin
280 and then wrapped with parafilm to avoid intrusion of the less viscous resin inside the pores.
281 The coated samples were placed with a sample holder connected to a permeameter built [at](#)
282 [Laboratoire Magmas et Volcans \(LMV, France\) in Clermont-Ferrand](#) following Takeuchi et al.
283 (2008). The measurements were performed at atmospheric pressure (i.e. without confining
284 pressure) and the samples were measured at a range of gas flow rates and upstream air
285 pressures to create a curve that could be fitted using a modified version of Darcy's Law, the
286 Forchheimer equation, to solve for viscous (k_1) and inertial permeabilities (k_2) (Rust and
287 Cashman, 2004, Lindoo et al. 2016 and Colombier et al. 2017).

288 Vesicle size distribution was performed following the method of Shea et al. (2010) and
289 Leduc et al. (2015), while the total crystallinity, the percentages for both crystal phases
290 (plagioclase and clinopyroxene) and size-populations (meso and microcrysts) were calculated
291 using the raw data from FOAMS program (Shea et al 2010) and the CSDcorrections program
292 of Higgins (2000) and the CSDslice data base (Morgan and Jerram 2006) to have the
293 percentage [of crystals in 3D with the corrected assumption for shape](#). We performed these

294 analyses on eight clasts picked up from each component-density distribution (stars in Figs. 6a
295 and 6b). The choice of the clasts was made mostly on the typologies, rather than on each
296 density distribution, in order to avoid the analysis of clasts with transitional characteristics.
297 For example, two golden pumice fragments were selected from the largest clasts that were the
298 less dense and didn't break, even if the values in vesicularity were similar. A larger number of
299 fluidal fragments were chosen (even if the density distribution was unimodal) because this
300 typology of clasts was the most abundant and was emitted all along the active fracture, so we
301 did our best in order to study products representative of the WF, the UF and the MV activities.
302 Only one spiny glassy and one spiny opaque were selected, because they were emitted only at
303 the MF. A full description of the textural ~~measurements~~measurements all performed at
304 ~~Laboratoire Magmas et Volcans (LMV)~~, as well as the raw data of these measurements are
305 available at DynVolc Database (2017).

306 **3.4 Bulk geochemistry**

307 For the determination of the bulk chemistry (Table S4 and Fig. 7) of the different pyroclasts
308 we selected the largest pyroclasts of golden pumice and the largest fluidal, spiny glassy and
309 spiny opaque scoriae (Table S4). We also analyzed two fragments of lava, from the beginning
310 and the end of the eruption (Table S4). Samples were crushed into coarse chips using a steel
311 jaw crusher and powdered with an agate mortar. Major and trace element compositions were
312 analyzed using powder (whole rock composition). In addition, for a sub-set of pyroclasts,
313 glass chips (2-5 mm in size) were hand-picked under a binocular microscope and analyzed
314 separately for trace elements. For major element analysis, powdered samples were mixed with
315 LiBO₂, placed in a graphite crucible and melted in an induction oven at 1050 °C for 4.5
316 minutes, resulting in a homogeneous glass bead. The glass was then dissolved in a solution of
317 deionized water and nitric acid (HNO₃), and finally diluted by a factor of 2000. The final
318 solutions were analyzed by ICP-AES. Trace element concentrations were analysed following
319 a method modified from Vlastélic et al. (2013). About 100 mg of sample (powder and chip)
320 were dissolved in 2 ml of 28M HF and 1 ml of 14M HNO₃ in teflon beaker for 36 hours at
321 70°C. Solutions were evaporated to dryness at 70°C. The fluoride residues were reduced by
322 repeatedly adding and evaporating a few drops of concentrated HNO₃, before being fully
323 dissolved in ca. 20 ml of 7M HNO₃. These solutions were diluted by a factor of 15 with
324 0.05M HF (to reach rock dilution factor of ca. 4000) and trace element abundances were
325 determined by quadrupole ICPMS (Agilent 7500). The analyses were performed in plasma
326 robust mode (1550 W). The reaction cell (He mode) was used to reduce interference on

327 masses ranging from 45 (Sc) to 75 (As). The signal was calibrated externally (every 4
328 samples) with a reference basaltic standard (USGS BHVO-2) dissolved as for the samples and
329 using the GeoRem recommended values (<http://georem.mpch-mainz.gwdg.de/>). For elements
330 that are not well characterized in literature (As, Bi, Tl), or which show evident heterogeneity
331 (e.g. Pb) in BHVO-2 powder, the signal was calibrated using the certified concentrations of a
332 synthetic standard, which was also repeatedly measured. The external reproducibility (2σ
333 error) of the method is 6% or less for lithophile elements and 15% or less for chalcophile
334 elements.

335 **3.5 Glass and crystal chemistry**

336 Spot analyses of matrix glass and crystal composition (Table S5) were carried out using a
337 Cameca SX100 electron microprobe (LMV), with a 15 kV acceleration voltage of 4 nA beam
338 current and a beam of 5 μm diameter for glass analyses. However, for the spiny opaque
339 scoria, characterized by abundant crystals with rapid growth textures, a voltage of 8 nA beam
340 current and a beam of 10 μm diameter were used. For this latter sample, 10 analyses per
341 sample were performed due to the heterogeneity within the highly crystallised glass (Fig. 8a),
342 while for the other samples 6 analyses per sample were enough to characterize the clean
343 homogeneous glass. For crystal analysis, a focused beam was used. For the characterization of
344 the meso- and micro-crysts, due to their small size, only two to three measurements were
345 performed, one at the edge, one in the middle and one at the core of the crystals, to check for
346 possible zonation.

347 **3.6 Melt inclusions**

348 Melt inclusions (MIs; Table S6, Figs. 8b and 9) were characterized in the olivine mesocrysts
349 from the three groups of scoriae (fluidal, spiny glassy and spiny opaque), but not in the
350 pumice group, because crystals were too rare and small to be studied for MIs.

351 Olivine crystals were handpicked under a binocular microscope from the 100– 250 and
352 250– 600 μm grain size fractions of crushed tephra. Crystals with MIs were washed with
353 acetone, embedded in epoxy and polished individually to generate adequate exposure of the
354 MIs for *in situ* electron probe microanalysis. The MIs are spherical to oblate in shape and
355 range in size from 10 to 200 μm . Some of the MIs contain shrinkage bubbles but all of those
356 studied are totally deprived of daughter minerals. Major elements were measured on a
357 Cameca SX-100 microprobe at LMV (Table S6). For major elements, the larger MIs were
358 analyzed with a spot diameter of 10-20 μm and sample current of 8 nA, whereas the smaller

359 MIs were analyzed with a beam of 5 μm and a sample current of 4 nA. The results are given
360 in Table S6, and analytical details and uncertainties are listed in Óladóttir et al. (2011) and
361 Moune et al. (2012).

362 **4 Results**

363 **4.1 Deposit texture (grain size, componentry, morphology) and petrological description** 364 **of the samples**

365 The pyroclastic deposits at the WF and UF sites (Fig. 1a) are formed by scattered
366 homogeneous smooth fluidal (Figs. 3d) bombs and lapilli scoria. The average dimension of
367 the fragments is around 4 cm (maximum axis) with bombs up to 10 cm and scoria lapilli up to
368 2 cm in size (Fig. 3e).

369 At the MV, the reversely graded deposit (Fig. 3b) is made up of lapilli and bombs, with
370 only minor coarse ash (Fig. 3c). The lower 5 cm at the base are very well-sorted and show a
371 perfect Gaussian distribution with a mode at 4 mm (Fig. 3c). In contrast, the grain size
372 distribution of the upper 5 cm is asymmetrical with a main mode coarser than 22 cm and a
373 second mode at 8 mm (Fig. 3c). This upper deposit is negatively skewed due to the abundance
374 of coarse clasts. The dataset shows a similarity between the grain size distributions of the
375 basal tephra ejected from the 2014 MV and the ones for the lava fountaining of the 2010
376 summit event (Fig. 3f and Hibert et al., 2015). On the contrary, the top of the 2014 fall differs
377 from fountain deposits, being coarser and polymodal, and it is ascribed to dominantly
378 Strombolian activity (Fig. 3f).

379 In terms of componentry of the deposits, four types of clasts were distinguished (Fig.
380 4): (i) golden pumice, (ii) smooth or rough fluidal scoriae, (iii) spiny glassy scoria, (iv) spiny
381 opaque scoria. The pumices are vesicular, ~~light-low-density~~ fragments, characterized by a
382 golden to light brown color, sometimes with a shiny outer surface (Fig. 4a). They are usually
383 rounded in shape. Golden clasts studied for textures contain a few microcrysts of plagioclase
384 (up to 0.1 mm in diameter), clinopyroxene up to 0.05-0.06 mm in diameter, and small olivine
385 up to 0.03 mm in diameter (Fig. 4), together with large areas of clean, light brown glass. The
386 fluidal scoria fragments have dark, smooth or rough shiny surfaces (Fig. 4b). They can be
387 more or less elongated in shape and have spindle as well as flattened shapes. The fluidal
388 fragments are characterized by rare mesocrysts of plagioclase and clinopyroxene and
389 microcrysts of plagioclase, clinopyroxene and olivine (Fig. 4b). The spiny glassy fragments
390 are dark, spiny scoria that range in shape from subrounded to angular (Fig. 4c). These

391 fragments contain abundant glassy areas, while the spiny opaque fragments lack a glassy,
392 iridescent surface. Both groups of spiny clasts are characterized by the presence of dark and
393 light brown glass. The spiny opaque fragments are the densest fragments and have the largest
394 amount of crystals. They contain, as the most abundant phase, relatively large meso- and
395 micro-crysts of plagioclase, up to 3 mm long, together with meso- and micro-crysts of
396 clinopyroxene and olivine (Figs. 4c and 4d). In the dark portions of their matrix, tiny fibrous
397 microcrysts of olivine + clinopyroxene + plagioclase + Fe-Ti oxides occur. The spiny glassy
398 fragments have the same crystal populations as the spiny opaque ones, but their plagioclases
399 are much smaller and attain a maximum length of only 0.3 mm. Clusters of plagioclase and
400 clinopyroxene are present in both the spiny opaque and the spiny glassy fragments, as well as
401 rare macrocrysts of olivine. The olivine macrocrysts exhibit the typical compositional (Fo
402 84.2) and petrographic features of olivine phenocrysts described in previous studies
403 (Clocchiatti et al., 1979; Albarede and Tamagnan, 1988; Bureau et al., 1998a and b; Famin et
404 al., 2009; Welsch et al., 2013). They are automorphic, fractured with oxides (mostly chromite)
405 and melt inclusions (Fig. 4c). Fluidal and pumice fragments studied for textures contain rare
406 macrocrysts and mesocrysts of olivine, and the crystals are essentially ~~microcrysts~~
407 The pumice and some fluidal fragments have lower contents of ~~microcrysts~~ than
408 some fluidal and spiny fragments, with the latter having the highest ~~microcryst~~
409 content (Table S4). For comparison two fragments of lava have been analyzed as well (Table
410 S3). The lava fragments are poorly vesiculated and completely crystalline (Fig. 4e). The lava
411 contains the same paragenesis of crystals described in the spiny opaque fragments, with the
412 main difference that its matrix is completely crystallized and constituted mostly by well-
413 formed plagioclase up to 800 microns and clinopyroxene up to 500 microns. Scarce, smaller
414 olivines, are also present Ubiquitous tiny rounded Fe-Ti oxides provide evidence of post
415 emplacement crystallization.

416 The componentry results are reported in Figure 5 for the MV deposits; being the
417 deposits from the WF and UF characterized exclusively by fluidal clasts (Fig. 3). At the base
418 of the MV deposit, the coarse fraction of the deposit is rich in golden and fluidal components
419 that represent more than 60-70 vol. % (Figs. 5a and 5b). The proportion of the two groups is
420 similar. In contrast, in the upper, coarse grained fall deposit, the clasts bigger than 8 mm are
421 dominated by the spiny scoria fragments, while the fraction smaller than 8 mm show a
422 dramatic increase in the golden and fluidal fragments, with the fluidal ones always more
423 abundant than the golden ones (Figs. 5a and 5b). Abundant ~~light~~ low-density, golden, coarse
424 lapilli pumice and bombs have been found scattered laterally up to 30 metres from the main

425 axis and were not found in the proximal deposit. On the basis of the high amount of pumice in
426 | the lower part of the deposit, we correlate the large, ~~light~~low-density clasts with the base of
427 | the proximal deposit, and consequently we interpret them as material emitted at the beginning
428 | of the June 2014 eruptive event.

429 **4.2 Particle density, porosity, connectivity, permeability and micro-texture**

430 Density analyses performed on 200 coarse lapilli reveal a large variation in density values
431 | from 390 kg/m^{-3} to 1700 kg/m^{-3} with a median value at 870 kg/m^{-3} (Table S3). The fragments
432 | collected from the MV have a bimodal density distribution, with a main population of ~~light~~
433 | low-density fragments having a mode at 800 kg/m^{-3} , and a second and denser population
434 | centered at 1400 kg/m^{-3} (Fig. 6a). The golden and fluidal fragments form the lower-density
435 | population and the spiny fragments are dominant in the denser population (Fig. 6a). For these
436 | samples there is a marked correlation between porosity and morphology, so that the spiny-
437 | opaque clasts are the densest (up to 1600 kg m^{-3} , with a vesicularity of 45 vol. %) and the
438 | golden pumice are the ~~lightest~~least dense (minimum density of 390 kg m^{-3} with a vesicularity
439 | of up to 86 vol. %; with a Dense Rock Equivalent density of ~~2.88880×10^3~~ kg m^{-3}). The
440 | fluidal fragments collected at the WF (Fig. 1b), have a density range from 700 to 1400 kg/m^{-3}
441 | and a mode at 1000 kg/m^{-3} (Fig. 6b). The five fragments from the only bomb collected at the
442 | UF are characterized by two distinct density values, the low density one ($700\text{-}800 \text{ kg/m}^{-3}$)
443 | refers to the core of the sample, while the high density one ($1400\text{-}1500 \text{ kg/m}^{-3}$) represents the
444 | quenched external rim of the bomb. Finally, the two fragments of lava show the highest
445 | density values at 1800 and 2150 kg m^{-3} . This last value is one of the highest found in the lava
446 | collected from 2014 up to 2017 (see Fig. 13 in Harris et al., 2017 and unpublished data).

447 In all these samples, the increase in vesicularity correlates with an increase in the
448 | amount of small (0.1 mm), medium (0.5-1 mm) and large (up to 4 mm) vesicles. In the fluidal
449 | clasts, these vesicles have a regular rounded or elliptical shape and are scattered throughout
450 | the sample. The ~~lightest~~low-density pumices are often characterized by the presence of a
451 | single, large central vesicle (10 – 15 mm) with the little vesicles and a few medium vesicles
452 | distributed all around it (Fig. 4). The spiny glass texture is characterized by a lower amount of
453 | ~~large~~small vesicles than in the pumice and by the presence of mostly medium sized vesicles,
454 | while the spiny opaque has more irregular shape, very large (up to 10 mm) vesicles with a
455 | small and a medium sized bubble population. In the spiny glass samples, the glass is more or
456 | less brown, with the dark brown portions being the ones with the lowest vesicle content and
457 | the highest microlitemicrocrysts content. The opaque samples have a central, very dark glass

458 portion, with low vesicle content, and a more vesicular glassy portion at the outer edges (Fig.
459 4). The two fragments of lava are poorly vesiculated (Fig. 6a) and characterized by large,
460 irregular vesicles (up to 5 mm in diameter). Clusters of small vesicles (up to 0.1 mm) are
461 scattered between the large ones.

462 The vesicle ~~s~~Size ~~d~~Distribution (VSD in Fig. 4) histograms ~~picture are characterized~~
463 ~~by a well the~~ decrease in percentage of vesicles from the golden to the lava as well as ~~the an~~
464 increase in coalescence and or expansion ~~signatures~~ in the spiny fragments, marked by the
465 increasing of the large vesicles population (Figs 4c and 4d). This trend is also marked by the
466 decrease in number of vesicle per unit of volume (N_v , Fig. 4) from the golden to the lava.
467 Finally, the trend is also mirrored by the total percentage of crystals (calculated in 3D, Fig. 4
468 and reported ~~both in 3D and 2D~~ for each sample in Table S3) that increases with the increase
469 of density of the clasts, from a minimum of 8 ~~vol. % in vol.~~ for the golden up to 55 ~~vol. % in~~
470 ~~vol.~~ for the spiny opaque scoria, and 100 ~~vol. % in vol.~~ for the lava (Fig. 4). Mesocrystals,
471 formed mostly by the same proportion of plagioclase and clinopyroxenes, are absent or very
472 scarce in the golden and fluidal fragments, while they reach their maximum values, up 21 ~~vol.~~
473 ~~% in vol.~~ in the spiny opaque fragment. The population of microcrystals is mostly constituted
474 by plagioclases that range from a minimum of 6 ~~vol. % in vol.~~ in the golden, up to 23-25 ~~vol.~~
475 ~~% in vol.~~ in the spiny fragments and to 64 ~~vol. % in vol.~~ in the lava.

476 The connectivity data (Fig. 6c) also indicate that the fluidal and golden clasts have a
477 larger amount of isolated vesicles (up to 40 ~~vol. % in volume~~) with respect to the spiny
478 products. The fluidal clasts from the WF are the most homogeneous with an average
479 percentage of isolated vesicles around 30 ~~vol. % in volume~~. In contrast, both the pumice and
480 the fluidal fragments from the MV, characterized by higher values of porosity ($> 75\%$), have a
481 wide range in percentage of isolated vesicles (between 20 and a few ~~percentage in volume~~
482 ~~%~~). The fragments of the bomb collected at the UF are consistent with a vesiculated core
483 characterized by scarce isolated vesicles and the quenched rind that has 30 ~~vol. %~~ of isolated
484 vesicles. Finally the spiny fragments have the lowest content of isolated vesicles (0-5 ~~vol. %~~
485 ~~in volume~~). Despite the presence of these isolated vesicles, all the samples show high values
486 of permeability, ~~with the Darcian (viscous, K_1) permeability values ranging from 10^{-11} to 10^{-10}~~
487 ~~m^2 (Fig. 6d and Table S3). The graph of vesicularity versus K_1 shows a slightly increase in~~
488 ~~permeability with vesicularity, being the golden pumice the most permeable among the~~
489 ~~samples and the spiny glassy fragment the least permeable. The three samples collected from~~
490 ~~the February 2015 eruption fit this trend. However, the densest spiny opaque scoria of the~~
491 ~~2014 eruption shares the high permeability value of the golden pumice.~~

492 4.3 Chemistry of the products

493 Major and trace element concentrations of whole-rock and hand-picked glass samples are
494 reported in Table S4. Whole rock major element composition is very uniform (e.g.,
495 $6.5 < \text{MgO} < 6.7$ wt%) and well within the range of Steady State Basalts (SSB), the most
496 common type of basalts erupted at PdF (Albarède et al., 1997). However, compatible trace
497 elements, such as Ni and Cr, are at the lower end of the concentration range for SSB
498 (< 100 ppm) indicating that the June 2014 eruption sampled relatively evolved melts. Ni and Cr
499 generally show higher concentrations in 2014 bulk rocks ($79 < \text{Ni} < 92$ ppm and $71 < \text{Cr} < 87$ ppm)
500 compared to the 2014 glass chips ($66 < \text{Ni} < 73$ ppm and $54 < \text{Cr} < 59$ ppm for all but two chips).
501 In the Cr vs Ni plot (Fig. 7a), whole rocks plot to the right of the main clinopyroxene +/-
502 plagioclase-controlled melt differentiation trend. This shift reflects the addition of Ni-rich
503 olivine (Albarède and Tamagnan, 1988). We estimate that the Ni excess results from the
504 occurrence of a low amount (0.7 to 1.3 wt%) of cumulative olivine in whole rocks, consistent
505 with thin section observations. The composition of olivine macrocrysts (ca. Fo₈₄) is too
506 magnesian to be in equilibrium with the low-MgO evolved composition of the 2014 magma.
507 Using our estimate for the amount of cumulative olivine, we recalculate the olivine-corrected
508 MgO content of the 2014 magma at 6.2 wt%. The June 2014 melt is thus only moderately
509 depleted in compatible elements compared to the previous eruption of December 2010
510 ($\text{MgO} \sim 6.6$ wt%, $\text{Ni} \sim 80$ ppm, $\text{Cr} \sim 120$ ppm). Conversely, the June 2014 melt is significantly
511 depleted in compatible elements compared to the earlier November 2009 eruption, which
512 sampled relatively primitive magmas (average $\text{MgO} \sim 7.7$ wt%, $\text{Ni} \sim 135$ ppm, $\text{Cr} \sim 350$ ppm)
513 (Fig. 7a). The 2014 evolved composition plots at the low-Ni-Cr end of PdF historical
514 differentiation trend (Albarède and Tamagnan, 1988), near the composition of lavas erupted
515 on 9 March 1998 after 5.5 years of quiescence (1992-1998). Note that olivine accumulation at
516 PdF generally occurs in melt having ca. 100 ppm Ni (Albarède and Tamagnan, 1988). Olivine
517 accumulation in evolved melts ($\text{Ni} < 70$ ppm) seems to be a distinctive feature of many small
518 post-2007 eruptions (e.g. this event and the three 2008 eruptions, see Di Muro et al., 2015).

519 A closer inspection of Ni-Cr variability in June 2014 whole rock samples (Fig. 7b)
520 reveals that scoria from the [Western Fracture WF](#) (140624-9b-6, Table S4) and early erupted
521 lavas (1406-21-1, Table S4) have the lowest amount of olivine ($< 0.9\%$) whereas scoria from
522 the [Upper Fracture UF](#) (140624-13a) and late erupted lavas (140324-12) have a slightly higher
523 amount of olivine ($> 1.2\%$). This is consistent with the general trends observed at PdF of
524 olivine increase from the start to end of an eruption (Peltier et al., 2009).

525 The so called “olivine control trend” in Ni-Cr space cannot be explained either by
526 addition of pure olivine, ~~(which contains less than 500 ppm Cr (Salaün et al., 2010; Di~~
527 ~~Muro et al., 2015; Welsch et al., 2009; Salaün et al., 2010; Di Muro et al., 2015)~~, or by the
528 addition of olivine plus pyroxene (which would require ca. 50% pyroxene with 970 ppm Ni
529 and 4800 ppm Cr, see Fig. 7 caption). Instead, addition of olivine hosting ca. 1% Cr-spinel
530 (with 25 wt.% Cr) accounts for data and observations, and is consistent with crystallization of
531 olivine and Cr-spinel in cotectic proportions (Roeder et al., 2006). The fact that some samples
532 (golden pumice) plot off the main, well-defined array, can be explained either by addition of
533 more or less evolved olivine crystals (within the range of Fo 80-85 measured in June 2014
534 samples) and/or slight variations ($\pm 0.02\%$) in the proportion of Cr-spinels (Fig. 7b).

535 The glass chemistry of the four clast types allows us to correlate porosity and oxide
536 contents and shows an increase in MgO from the spiny opaque to fluidal and golden
537 fragments (Fig. 8a). Consistent with petrological and textural observations, the spiny opaque
538 is the most heterogeneous type of clast in terms of glass composition (Fig. 8). The glassy
539 portion at the edge of the clast is similar to the spiny glass, while the interior, characterized by
540 dark areas rich in tiny fibrous microcrysts, shows scattered glass compositions with very low
541 MgO content as well as a decrease in CaO (Fig. 8). We attribute the significant variation in
542 glass composition within the different components to variable degrees of micro-crystallisation
543 as the bulk chemistry of all clasts is very similar and globally homogeneous.

544 **4.4 Melt inclusions**

545 MI analyses must be corrected for post-entrapment host crystallisation at the MI - crystal
546 interface. We used a $K_d = (\text{FeO/MgO})_{\text{ol}} / (\text{FeO/MgO})_{\text{melt}} = 0.306$ (Fisk et al., 1988; Brugier,
547 2016) and an average $\text{Fe}^{3+}/\Sigma\text{Fe}_{\text{total}}$ ratio of 0.11 (Bureau et al., 1998a; Di Muro et al., 2016 and
548 references therein) defined for PdF magmas. For the June 2014 melt inclusions, the post
549 entrapment crystallization (PEC) ranges from 2.9 to 10.5 wt%. Raw and corrected major and
550 volatile element concentrations of MIs are reported in Table S6.

551 Host olivines span a large compositional range from Fo₈₀ to Fo₈₆. Despite the evolved
552 bulk composition of the magma, most olivines are quite magnesian (Fo₈₃₋₈₅) and are not in
553 equilibrium with the evolved host magma. On the contrary, Mg-poor olivines (Fo₈₀₋₈₁) can be
554 considered as being in equilibrium with the bulk rock composition. The corrected
555 compositions of MIs in phenocrysts from the different samples partly overlap with the
556 evolved bulk rocks (MgO_{wr}: 6.1-7.2 wt%) and extend to higher MgO contents of up to 8.8

557 wt% (Table S6). MIs display a narrow range of transitional basaltic compositions ($K_2O= 0.5-$
558 0.9 wt%) and show no significant difference between the three types of scoriae. The major
559 element composition of melt inclusions correlates with that of the host olivines. Melt
560 inclusions in the high Fo-olivines have the highest MgO, CaO and TiO_2 and lowest K_2O
561 concentrations (Table S6). It is interesting to note that the June 2014 products contain two
562 populations of magnesian ($Fo_{>83}$) olivines hosting melt inclusions with two distinct Ca
563 contents. Most of the magnesian olivines contain MIs with unusually high CaO contents (11.6
564 – 12.9 wt%) and high CaO/Al_2O_3 ratios (0.8-0.9), higher than that of the bulk rocks (0.8) (Fig
565 8). The occurrence of olivines with “high Ca” melt inclusions has been observed in all three
566 different types of scoriae. A few magnesian olivines and all Mg-poor olivines ($Fo_{80.5-83.6}$) host
567 MIs with lower CaO contents (11.4 wt%). This latter composition overlaps with that of the
568 bulk rock (Fig 8). The “high Ca” population of inclusions is also enriched in TiO_2 and Al_2O_3
569 and depleted in MgO, FeO_T and Na_2O for a given olivine Fo content with respect to the “low
570 Ca” population. Both low- and high-Ca populations of melt inclusions have similar K_2O
571 contents and total alkali content increases from 3 wt% at 12.6 wt% CaO, to 3.5 wt% at 10.8
572 wt% CaO. However, we remark that high Ca melt inclusions from the June 2014 activity
573 record a significant scattering in K_2O contents, which range from 0.55 to 0.9 wt%. These
574 anomalous compositions potentially track processes of crystal dissolution (e.g. pyroxene
575 dissolution).

576 MIs in olivines from June 2014 can best be compared with those of other recent small-
577 volume and short-lived eruptions which emitted basalts with low phenocryst contents, like
578 those in March 2007 ($0.6 \times 10^6 m^3$) and November 2009 ($0.1 \times 10^6 m^3$) (Roult et al., 2012).
579 March 2007 aphyric basalt has a bulk homogeneous composition with intermediate MgO
580 content (MgO_{wr}: 7.33 wt%; K_2O : 0.67 wt%). Their olivines (Fo 81) are in equilibrium with
581 the bulk rock and their composition is unimodal (Di Muro et al., 2014). November 2009
582 products are the most magnesian lavas emitted in the 2008-2014 period, slightly zoned
583 (MgO_{wr}: 7.6-8.3 wt%; K_2O : 0.75 – 0.62 wt%) and contain a few percent of normally zoned
584 olivine macrocrysts with bimodal composition (Fo81 and Fo83.5, see Di Muro et al., 2016).
585 June 2014 bulk rocks (MgO_{wr}: 6.7 wt%; K_2O : 0.75 wt%) and melt inclusions in Fo_{80-81}
586 olivines are quite evolved. Their composition is close to that of products emitted by summit
587 intracaldera eruptions in 2008, ca. 1.5 years after the large 2007 caldera forming eruption (Di
588 Muro et al., 2015) (Fig. 8). As already reported for 2008 products, many olivine macrocrysts
589 of 2014 are clearly too magnesian to be in equilibrium with the relatively evolved host melts.
590 Overall, MgO content in 2007-2014 melt inclusions tends to decrease with decreasing Fo

624 (An_{76.5-79.5} and An_{63.1-72.9}, Fig. 10a). Similar bimodal distributions were observed in many
625 other products, at PdF (Di Muro et al., 2015). Mesocrysts (An_{75.5}Ab_{23.8}Or_{0.7} on average) are
626 more calcic with respect to microcrysts (An_{65.7}Ab_{33.1}Or_{1.2} on average). Normal zoning is
627 found from plagioclase cores to rims (Fig. 10a). The composition and zonation of 2014
628 plagioclases clearly contrast with the complex and often reverse zoning patterns and
629 intermediate composition of the 2008 PdF products that were attributed to pre-eruptive
630 magma heating (Di Muro et al., 2015).

631 Plagioclase-melt equilibrium and melt composition in pyroclastic rocks and water-
632 quenched lavas were used to estimate both temperature and water content dissolved within the
633 melt (Fig. 10b and Table S5). Temperature estimates are based on the (dry) equation of Helz
634 and Thornber (1987) recalibrated by Putirka (2008). Dissolved water content was calculated
635 from the plagioclase hygrometer of Lange et al. (2009) at 50 MPa. This pressure corresponds
636 to the average CO₂-H₂O saturation pressure (recalculated with Papale et al., 2006) typically
637 recorded in melt inclusions from central products at PdF (e.g. 1931 eruption in Di Muro et al.,
638 (2016) and references therein). This pressure roughly corresponds to the sea level depth,
639 which is inferred to be the location of the potential main shallow magmatic reservoir (Peltier
640 et al., 2009; Lengliné et al., 2016; Coppola et al., 2017). The application of the plagioclase
641 hygrometer of Lange et al. (2009) makes it possible to estimate the dissolved water content in
642 the melt with a nominal uncertainty of 0.15 wt% and is only slightly dependent on pressure.
643 Plagioclase compositions not in equilibrium with the melt (glass or bulk rock) are those of
644 mesocryst cores with the highest (An_{>76.5}) anorthite content (Fig. 10a and Table S5). Such
645 compositions are more in equilibrium with CaO-richer magnesian melts than those measured
646 in matrix glasses and bulk rocks of 2014 eruption and likely formed during early stages of
647 shallow magma differentiation (Fig. 10a).

648 In order to determine pre-eruptive conditions, calculations were performed only on
649 paired plagioclase rims and matrix glasses in equilibrium, using the plagioclase-melt
650 equilibrium constant of Putirka (2008) calibrated for melts whose temperature exceeds
651 1050°C ($K_{d_{An-Ab}} = 0.27 \pm 0.05$). Our review of published and unpublished data shows that melt
652 temperature progressively decreases from April 2007 (1188 \pm 16 °C) to January-October
653 2010 (1147 \pm 9°C) and positively correlates with K₂O content in melts which increases from
654 0.70 to 0.96 wt% (Fig. 10b). The melts from the June 2014 eruption record the lowest
655 temperatures in post-2007 eruptions (1131 \pm 15 °C) together with the highest K₂O-enrichment
656 (K₂O: 0.90 \pm 0.12 wt%). The lowest temperatures are recorded by spiny scoriae, while the
657 temperature of golden scoriae overlaps with that of 2010 products emitted before the 2010-

658 2014 phase of quiescence. In spite of the large variability in melt composition and
659 temperature, average pre-eruptive water content dissolved in the melts (0.5 ± 0.2 wt%) is
660 quite homogeneous for the whole 2008-2014 period. In 2014, the lowest estimated dissolved
661 water content (down to 0.38 wt%) is for the golden and some fluidal scoriae, while the
662 maximum amount (0.68 wt%) is for the spiny opaque scoriae. However, water content
663 estimated from core-bulk rock equilibrium (0.3 ± 0.1 wt%) is slightly lower than that estimated
664 from rim and microlite-matrix glass equilibrium (0.5 ± 0.2 wt%), but the difference broadly
665 overlaps the nominal uncertainty related to calculations. Dissolved water contents in melts of
666 the pyroclasts are thus intermediate between those measured in 2007 melt inclusions (H_2O :
667 0.8 ± 0.15 wt% and up to 1.1 wt%) and those typically found in degassed matrices of lava
668 and Pele's hairs of 2007 (Fig. 10b; 0.2 wt%; see Di Muro et al., 2015; 2016).

669 5 Discussions

670 5.1 Eruptive dynamics

671 The activity fed by the uppermost WF and UF (Fig. 1) was very short-lived, as shown by the
672 presence of only scattered bombs and coarse lapilli (Figs 3d and 3e). The homogeneity of
673 these clasts, their coarse grained nature and the fluidal smooth texture are in agreement with
674 very short-lived fire-fountaining/magma jets. Glassy outer surfaces of clasts have been
675 interpreted as a late-stage product of fusion by hot gases streaming past the ejecta within the
676 jet/fountain (Thordarson et al., 1996; Stovall et al., 2011). However, the occurrence of this
677 process is not supported by the homogeneous glass composition in our fluidal clasts.
678 Therefore, we interpret these features here just as rapid quenching and not re-melting.
679 Vlastélic et al. (2011) ~~have~~ documented the mobility of alkalis and other elements on PDF
680 clasts ~~that experienced~~ that experienced long exposures to acid gases. In the 2014 eruption
681 pyroclasts, the mobility of elements was ~~is~~ prevented by the short duration of the events.

682 At lower altitude and close to the MV (Fig. 1), the 5 cm layer at the base of the fall
683 deposit is fine-grained (Figs. 3b and 3c), rich in fluidal and golden fragments (Fig. 5), with a
684 perfect Gaussian grain size curve (Fig. 5), and similar to that reported from the weak 2010
685 fountaining event (Fig. 3f and Hibert et al., 2015). Therefore, we interpret this deposit as
686 being due to weak Hawaiian like fountaining (sustained, but short-lived) activity. We want to
687 remark here that this activity happened during the night and was not observed. The top of the
688 same deposit is coarse grained (Figs 3b and 3c), bimodal, has a lower content in coarse ash
689 (Table S2) and is rich in spiny opaque and spiny glass fragments (Fig. 5). The reverse grain

690 size likely records the transition from early continuous fountaining to late discrete
691 Strombolian activity (observed and recorded on the 21 of June 2014, Fig. 2). This transition in
692 activity is typical of many eruptions at PdF (Hibert et al., 2015). The reverse grading of the
693 whole deposit (Figs. 3b and 3c) is thus not correlated with an increase in energy of the event,
694 but with two different eruptive dynamics and fragmentation processes. The decrease in coarse
695 ash, which correlates with the decrease in energy of the event, highlights the most efficient
696 fragmentation process within the Hawaiian fountaining with respect to the slow gas ascent
697 and explosion of the Strombolian activity. These conclusions are consistent with (i) the
698 continuous and progressive decrease in intensity of Real time Seismic Amplitude
699 Measurement recorded by the OVPF seismic network (unpublished data), and (ii) satellite
700 derived TADR which suggest continuous decay of magma output rate after an initial short-
701 lived intense phase (Coppola et al., 2017).

702 **5.2 Interpretation of the different textural signatures and the meaning of the 4 typologies** 703 **of clasts.**

704 1) Background on the texture of clasts from Hawaiian and Strombolian activities

705 The first microtextural analysis of Hawaiian ejecta was performed by Cashman and Mangan
706 (1994) and Mangan and Cashman (1996) on pyroclasts from 1984 to 1986 Pu'u Ō'ō
707 fountainings. The authors defined two clast types: 1) 'scoria' consisting of closed-cell foam of
708 $\leq 85\%$ vesicularity, with round, undeformed, broadly-sized vesicles, and 2) 'reticulite', an
709 open-cell polyhedral foam with $\sim 1 \mu\text{m}$ thick vesicle walls with $>95\%$ vesicularity. They stated
710 that the scoria to reticulite transition is a consequence of Ostwald ripening, where larger
711 bubbles grow at the expense of smaller bubbles due to post-fragmentation expansion of clasts
712 within the fountain. According to this model, scoria preserves textures closer to conditions at
713 fragmentation, whereas continued vesiculation and clast expansion in the thermally-insulated
714 core of the fountain results in reticulate. This model was confirmed at lava fountains at Etna
715 (Polacci et al., 2006), Villarrica (Gurioli et al., 2008), Kīlauea Iki, (Stovall et al., 2011 and
716 2012), Mauna Ulu (Parcheta et al., 2013) and Al Madinah (Kawabata et al., 2015). These last
717 authors also measured the connected and isolated porosity in the AD1256 Al-Madinah
718 Hawaiian fountaining eruptions. They found that the reticulite-like textures from the central
719 part of these very high fountains showed isolated vesicles in agreement with low shear rates
720 and low viscosity melts, where bubbles may grow spherically and remain isolated. In contrast,
721 at margins of the fountains, high shear may lead to stretching and mechanical coalescence of

722 bubbles, forming the common, fluidal types of particles seen also in the deposits. They also
723 stated that lower vesicularity and greater isolated porosity were found in some tephra
724 interpreted as resulting from violent Strombolian eruptive phases.

725 The data that we found in our study of the typical activity of PdF agree only partially
726 with all these interpretations. The reason is that we sampled and measured products of very
727 weak Hawaiian to Strombolian activities. If we plot the approximate durations and masses of
728 these events on the Houghton et al. (2016) diagram, the 2014 activity of PdF falls into the two
729 fields for transient and fountaining activity, but at the base of the diagram. We here show for
730 the first time that short lived and weak fountaining can preserve pyroclast textures that record
731 magma ascent and fragmentation conditions before the explosions and also provide some
732 information about the pre-eruptive storage conditions. The occurrence of time-variable ascent
733 conditions is also reflected in the time evolution of eruptive dynamics, with the golden and
734 fluidal scoriae emitted from the low Hawaiian fountaining episodes and the spiny fragments
735 from the Strombolian-like explosions

736 2) The four typologies of clasts and their distribution in space and in time in the 2014
737 eruption at PdF

738 So, as described in 5.1, longitudinal variation in eruptive style along the fracture system
739 produces a spatial variability in the proportions of the four typologies of clasts. The
740 uppermost fractures (~~Western and Upper Fractures~~ WF and UF, Fig. 1a) are characterized
741 solely by fluidal fragments (Fig. 4b); they lack both the spiny and the golden components. In
742 addition, these fluidal clasts are the ones showing the smoothest surfaces (indicative of rapid
743 quenching in a very hot environment), low porosity values (between 50 to 77 vol. %, Fig. 6b),
744 the highest content in isolated vesicles (~ 30 vol. % ~~in vol.~~ Fig. 4c), and low vesicle numbers
745 (3 to 5 x 10⁶, Fig. 4b), comparable to the spiny fragments. They have scarce mesocrysts (1-2
746 vol. % ~~in vol.~~ Table S3) and very low amount of microcrysts of plagioclase and clinopyroxene
747 (3 to 11 vol. % ~~in vol.~~, Table S3). These fluidal scoria fragments were emitted by short lived
748 jets of magma, therefore they underwent rapid quenching in a very hot environment that
749 prevented any expansion or further vesiculation and preserved a very high number of isolated
750 vesicles (Fig. 6d). Syn-eruptive crystallization was hindered by high ascent velocities in the
751 dyke, due to the sudden release of over-pressure in the shallow magma reservoir.

752 The four typology of clasts, golden pumice, fluidal scoria and the spiny fragments
753 (Fig. 4), were found associated only at the MV. The relative proportions of these fragments
754 four typologies of clasts correlate with the eruptive dynamics. T, ~~being~~ the golden lapilli and

755 fluidal clasts were in fact dominant in the Hawaiian, more energetic activity at the beginning
756 of the eruption (during the night between the 20 and the 21 of June 2014). In contrast, ~~and~~ the
757 spiny fragments were dominant during the Strombolian activity, coinciding with the
758 decreasing in Mass Discharge Rate (MDR, early in the morning of the 21, Fig. 2 and Coppola
759 et al., 2017). The golden and fluidal fragments from the MV show the highest porosity (86 %,
760 Fig. 6a), variable proportions of isolated vesicles (Fig. 6c) and high, but variable, N_V numbers
761 (Figs. 4a). They are also characterized by a uniform vesicle size population with clear
762 evidence of incipient expansion, especially in the fluidal fragments (Figs. 4a and 4b). From
763 the connectivity graph, there is a clear decrease in isolated vesicles with the increase in
764 vesicularity (Fig. 6c). The content in crystal, mostly formed by microcrysts of sodic
765 plagioclase (Fig. 10a) due to magma degassing during its ascent and decompression in the
766 conduit (Di Muro et al., 2015), is very low, especially in the golden pumice (up to 15 vol. %
767 ~~in vol.~~), and slightly higher for the fluidal clasts (up to 23 vol. % ~~in vol.~~). We interpret the
768 golden fragments, at the MV, to be the fastest (low amount of microcrysts) and less degassed
769 magma (high vesicularity coupled with high N_V), which experienced only a very short
770 residence time in the magma transport system (dyke+vent), followed by the fluidal fragments.
771 In contrast the spiny fragments, characterized by higher percentage of microcrysts and
772 mesocrysts, by the lack of isolated vesicles, by the presence of coalescence signature and low
773 N_V values (Figs. 4c and 4d), are indicative of an extensively degassed and cooled magma. The
774 presence of the mesocrysts (that formed in the shallow reservoir) in the spiny fragments, and
775 their slightly cooler temperature (Fig. 10b), strongly support this interpretation. The spiny
776 fragments likely record the slowest ascent velocity and the longest residence time in the
777 reservoir+dyke+vent system compared to the golden/fluidal counterpart. Therefore these
778 fragments are associated with Strombolian events, and decreasing MDR, in agreement with
779 their slower ascent that allows extensive syneruptive crystallization.

780 Among spiny fragments, the opaque ones are the densest, they lack a uniform glassy
781 surface, and they are characterized by i) very high microcryst content, ii) strong
782 coalescence signature (Fig. 4d), iii) heterogeneous glass chemistry, and iv) mingling with
783 hotter magma at the clast edges (Fig. 8a). All these features reveal the composite nature of
784 these clasts. We interpret the spiny opaque as spiny glass fragments recycled inside the
785 eruptive vent during the explosions, being the densest portion of the magma prone to fall back
786 in the vent/fracture (Fig. 2b).

787

788 *3) Degassing-driven versus cooling-driven crystallization*

789

790 | Syn-eruptive degassing is favoured by bubble connectivity/permeability (Figs. 6c and 6d) in
791 | the ascending magma, enhanced by syn-eruptive crystallisation in the conduit (especially
792 | microcrysts of plagioclase, Fig. 10a), even for magmas at low vesicularity. However, our
793 | dataset also supports the occurrence of magma stratification in the reservoir. Textural and
794 | petrological data demonstrate that the initial activity emitted a small volume of melt
795 | (represented by golden and large part of the fluidal fragments) with very scarce crystals. This
796 | crystal-poor melt was followed in time by the main volume of magma that contains a larger
797 | amount of mesocrysts (spiny clasts and lava). Lava flows represent the main volume emitted
798 | in the 2014 eruption. Mesocrysts are absent in the golden, scarce in the fluidal and more
799 | abundant in the spiny (Figs 4b, 4c and 4d) and lava (Fig. 4e) fragments and consist in an equal
800 | percentage of plagioclase and clinopyroxene and minor olivine. Their composition indicates
801 | that they formed in the reservoir, as shown by their different composition in respect to the
802 | microcrysts counterparts (Fig. 10a) that formed during melt degassing in the conduit (Fig.
803 | 10a). Most important, a large amount of microcrysts in lava formed in the reservoir as well
804 | during magma cooling (Figure 10a). So, we have a range of crystallization conditions. The
805 | fact that the lighter plagioclase are not concentrated in the upper and early erupted portion of
806 | the reservoir can be due either to the fact that often they are locked in clusters with the
807 | clinopyroxene or that this melt was expelled from the crystal-rich portion of the reservoir (see
808 | Figure 10b). Water exsolution from the melt can result from its extensive crystallization,
809 | which induces an increase in dissolved volatile content, up to saturation (second boiling) and
810 | can drive melt-crystal separation.

811 | In conclusion, the crystals in the 2014 fragments do reflect the shallow reservoir
812 | conditions and the ascent degassing processes.

813

814 | 4) Textural syn-eruptive versus post fragmentation modifications

815

816 | To prove that the 2014 vesiculation of the clasts have been not modified by post
817 | fragmentation expansion process, following Stovall et al. (2011), we use a plot of vesicle-to-
818 | melt ratio (V_G/V_L , after Gardner et al., 1996) and vesicle number density (N_V , Fig. 11). As
819 | demonstrated by Stovall et al. (2011), addition of small bubbles leads to an increase in N_V and
820 | only a slight increase in V_G/V_L . Bubble growth by some combination of diffusion and
821 | decompression leads to an increase in V_G/V_L at constant N_V . N_V decreases while V_G/V_L
822 | increases during bubble coalescence, whereas loss of bubbles via collapse or buoyant rise

823 leads to a reduction in both parameters. Intermediate trends on the diagram reflect
824 combinations of more than one of these processes. The pumice and the scoria from the MV of
825 PdF show the highest V_G/V_L , but also the highest N_V , suggesting preservation of small
826 vesicles and growth by some combination of diffusion and decompression. The presence of
827 the small vesicles and the lack of a strong coalescence/expansion signature confirm that the
828 weak PdF activity leads to only limited post-fragmentation expansion inside the hot portions
829 of the short-lived fountains. These data contrast with the data from the more energetic
830 fountaining events observed at Kilauea or elsewhere, where pre-eruptive information is
831 basically erased because pumice textures are dominated by expansion effects due to their
832 longer residence within the long-lived energetic fountaining. In contrast, the densest, spiny
833 scoriae and the scoria from the Fractures activity show the lowest values of N_V and V_G/V_L ,
834 due to incipient coalescence and/or loose/lack of small bubbles.

835 According to previous works (listed above), the golden pumice of PdF should be
836 derived from the central part of the fountains, but they do not show the strong post expansion
837 signatures reported ~~in the literature~~ [by other samples collected from more energetic Hawaiian](#)
838 [fountainings](#) -(Fig. 11). It is interesting to note that the fluidal fragments at the MV are less
839 smooth (Fig. 4), more vesiculated, and have a lower content of isolated vesicles than the
840 fluidal scoria from the uppermost Fractures (Fig. 6). Therefore fluidal fragments at the 2014
841 MV could indeed represent clasts that have been partly modified during their residence in the
842 external part of the fountains, while the golden samples could come from the central part
843 (Stovall et al., 2011 and 2012). However, the slight differences in crystallinity and glass
844 chemistry between the fluidal and golden fragments support the idea that each of these
845 fragments has an imprint from the pre-fragmentation setting. In contrast, the spiny fragments
846 from the MV and the fluidal fragments from the Fractures show low N_V and low V_G/V_L in
847 agreement with loss of vesicles and coalescence. However, the presence of large numbers of
848 isolated vesicles within the fluidal scoria from the Fractures agrees with their provenance
849 from a fast hot ejection of relatively degassed magma (low N_V). In contrast the spiny
850 fragments, especially because of the presence of abundant mesocrysts and increase in
851 syneruptive microcrysts, are indicative of the slowest ascent velocity and extensively
852 degassing and cooled magma. The spiny fragments are the most degassed, densest and the
853 most crystal rich magma that was emitted during low-energy activity by Strombolian
854 explosion, where recycling phenomena were also very frequent (Fig. 2f).

855 Our vesicle connectivity results are in full agreement with the recent review of
856 Colombier et al. (2017b). According to these authors, connectivity values can be used as a

857 useful tool to discriminate between the basaltic scoria from Hawaiian (fire fountaining) and
858 Strombolian activity. The broad range in connectivity for pumice and scoria from fire
859 fountaining is interpreted simply as being due to variations in the time available before
860 quenching due to differences in location and residence time inside the fountain. The fluidal
861 fragments from the WF are the richest in isolated vesicles because they are transported by
862 very short lived hot lava jets. In contrast, the higher connectivity observed in scoria from
863 Strombolian activity is probably related to their higher average crystallinity, and more
864 extensive degassing prior to the eruption; (Colombier et al., 2017b). The spiny surface of
865 these Strombolian fragments is due to the fact that these weak explosions emit only a small
866 solid mass fraction and the partially quenched dense clasts land quickly after a short cooling
867 path through the surrounding atmosphere (e.g. Bombrun et al., 2015).

868 All the clast, from golden to spiny, are very permeable, independent on their
869 vesicularity, crystal content and/or of the presence of isolated vesicles. This is in agreement
870 with our interpretation that magma degasses during its ascent in the conduit and that promotes
871 microlite nucleation (see the sodic plagioclase, Fig. 10a) before magma fragmentation (see
872 also Di Muro et al. 2015 with the Pele's hairs and tears samples for the three 2008 eruptions).
873 Moreover, we always find that some of the spiny clasts (especially the opaque ones) are
874 slightly less permeable than the golden and fluidal ones, but not ~~as impermeable with a low~~
875 permeability as we would expect by their low vesicularity.

876 In conclusion, we can state that i) the crystals lower the percolation threshold and
877 stabilize permeable pathways and ii) this is true for the syn-eruptive sodic plagioclase that
878 favor an efficient degassing in the relatively crystal-rich magma, because of their low wet
879 angles that favor degassing against nucleation (Shea, 2017) and their aspect ratio (e.g. Spina
880 et al. 2016) iii) therefore permeability develops during vesiculation through bubble
881 coalescence, which allows efficient volatile transport through connected pathways and
882 relieves overpressure (Lindoo et al., 2017). Pervasive crystal networks also deform bubbles
883 and therefore enhance outgassing (Oppenheimer et al., 2015). Based on Saar et al. (2001)
884 crystals should start to affect the behavior of the exsolved volatile phase when they approach
885 20 vol. % (Lindoo et al., 2017). In our dataset, apart from the golden and part of fluidal, all
886 the other clasts do have microcrystals >20%. Our data completely support that slow
887 decompression rate allows more time for degassing-induced crystallization, which lowers the
888 vesicularity threshold at which bubbles start to connect.

889 Rapid re-annealing of pore throats between connected bubbles can happen due to short
890 melt relaxation times (Lindoo et al; 2016). This phenomenology could explain the high

891 amount of isolated vesicles in the fountaining samples. However, vesicle distributions of the
892 golden and fluidal fragments are almost perfect Gaussian curves, so it seems that if the
893 relaxation process happens it just merged perfectly with the expected vesicle distribution. In
894 contrast, coalescence and/or expansion (as we observe in the spiny fragments) do not fit the
895 curves (Fig. 4). In addition, we should expect that in crystal-poor fragments, due to melt
896 relaxing and pathways closure, the clasts became almost impermeable after quenching, as
897 revealed by some petrological experiments performed on crystal-poor basaltic magma
898 (Lindoo et al., 2016). In contrast, in high crystalline magmas, the presence of micro-crystals
899 increases viscosity thus preserving the coalesced textures (see Moitra et al., 2013). The
900 isolated vesicle-rich fragments of the 2014 PdF eruption are highly permeable, and are
901 characterized by variable ranges of porosity and numbers of vesicles (Fig.4 and Fig. 6d) that
902 seem more related to the pre-eruptive conditions than to the post relaxation of low-viscosity
903 melts. In the 2014 crystal-poor samples, the permeability increases rapidly once the
904 percolation threshold has been reached, and efficient degassing prevents bubble volumes from
905 expanding past the percolation threshold (Rust and Cashman 2011).

906 In conclusion, also the vesicles in the 2014 fragments do partly reflect the shallow
907 reservoir conditions and mostly the ascent degassing processes.

908

909 **5.4 Integration between the physical and textural characteristics of the products and** 910 **their geochemical signature: insight into the feeding system**

911 According to Peltier et al. (2016), the June 2014 eruption emitted magma from a shallow
912 pressurized source located only 1.4-1.7 km below the volcano summit. Coppola et al. (2017)
913 suggest that the 2014 event was fed by a single shallow and small volume magma pocket
914 stored in the uppermost part of the PdF central plumbing system. All 2014 clasts show
915 homogeneous and evolved bulk compositions, irrespective of their textural features. June
916 2014 products are among the most evolved products erupted since at least 1998 and are
917 moderately evolved with respect to those emitted in 2010, just before the 2010-2014
918 quiescence. Bulk rock and melt inclusion data suggest that the 2014 evolved magma can be
919 produced by crystal fractionation during the long lasting (4.6 years) storage and cooling of the
920 magma injected and partly erupted in November 2009. The different types of scoria and
921 pumice emitted in 2014 show significant variations in glass composition (Fig. 8b) due to
922 variable degrees of micro-crystallization. In theory, microcrysts can reflect late stage (during

923 magma ascent and post-fragmentation) crystallization. In this case, their variable amount
924 within, for instance, the glassy and opaque parts of the spiny scoria might reflect slower
925 ascent velocity or longer residence time in the system (e.g. Hammer et al., 1999, Stovall et al.,
926 2012; Gurioli et al., 2014) in agreement also with the vesicle signature. However, the four
927 typologies of clasts differ also in terms of mesocryst content (from rare to 5 vol. % for the
928 golden and fluidal and 14-23 vol. % for the glassy spiny and spiny opaque, respectively).
929 Equilibrium plagioclase-melt pairs record an almost constant and moderate dissolved water
930 content, intermediate between that expected for melts sitting in the main shallow reservoir
931 (located close to sea level) and the degassed matrix of lavas. Dissolved water contents are
932 thus consistent with pre-eruptive magma water degassing during its storage at shallow level,
933 as suggested by geophysical data, and suggest that the plagioclase mesocrysts and some of the
934 microclites-microcrysts in the spiny scoria and in the lava grew during magma storage (Fig.
935 10a). Melt composition records a potential pre-eruptive thermal gradient of ~30 °C between
936 the hotter (pumice and fluidal) and the cooler (spiny) magma (Fig. 10b).

937 Tait et al. (1989) suggest that magma evolution can lead to oversaturation of volatile
938 species within a shallow reservoir and trigger a volcanic eruption. At PdF, the golden and the
939 fluidal clasts might represent the portion of magma located at the top of the shallow reservoir
940 and enriched in bubbles of water rich fluids, released by the cooler, more crystallized and
941 more degassed “spiny-lava” magma (Fig. 10b). The small volume of magma, its constant bulk
942 composition and the very small inflation recorded prior to the eruption (Fig. 1d) could be
943 consistent with an internal source of over-pressure related to volatile exsolution. Larger
944 inflation rates over a broader area are expected when shallow reservoir pressurization is
945 related to a new magma input from a deeper source. Slight baseline extensions both on distal
946 and proximal sites suggest that magma transfer towards shallower crustal levels started short
947 before (11 days) the final magma eruption. Geochemical data do not support the occurrence of
948 a new magma input in the degassed and cooled 2014 reservoir. We can thus speculate that
949 stress field change related to progressive deep magma transfer has promoted volatile
950 exsolution, melt-crystal separation and melt expansion in the shallow reservoir. Textural
951 heterogeneity of the 2014 products partly reflects a pre-eruptive physical gradient recorded by
952 the variability in crystal and bubble contents in the shallow reservoir feeding this eruption.
953 The golden and fluidal fragments are the bubble richer and hotter portion of the melt. The
954 spiny fragments are the degassed and cooler portion of the reservoir, whose progressive
955 tapping led to a decrease in explosive intensity (from fountaining to Strombolian activity).
956 Our results are also consistent with processes of mechanical reservoirs/dyke stratification, as

957 observed by Menand and Phillips (2007). As explained earlier, magma ascent promoted
958 syneruptive degassing induced crystallization. The spiny opaque clasts can be considered as
959 being recycled material that fell back into the system. Accumulation of olivine crystals out of
960 equilibrium with the host magma produces minor variations in mesocryst contents as
961 observed within the same type of clasts sampled at different times/locations during the
962 eruption, with the scoria from the WF and early erupted lava being the ones with the lowest
963 amount of olivine (Table S4 and Fig. 7b). Again, this temporal variation supports an increase
964 in large heavy crystals within the most degassed magma emitted toward the end of activity,
965 further suggesting that it corresponds to the lower part of the reservoir.

966 Our dataset permits us to propose that the 2014 eruption was fed by a physically zoned
967 magma reservoir. The ~~lighter-low-density,~~ crystal-poor, bubble-rich magma located in the
968 upper part of the storage system at reservoir, ~~top~~-ascended first, rapidly and fed the early,
969 more energetic phase, the Hawaiian fountaining. This ~~lighter-low-density~~ magma is not more
970 evolved than the spiny one (same bulk compositions) and it is not necessarily richer in
971 dissolved volatile amounts; it is just poorer in crystal and richer in bubbles. Second boiling,
972 possibly triggered a few days before the eruption by stress field change, is responsible of the
973 extraction of bubble rich melt from a crystal-rich network. This last one ~~is-will~~ represented by
974 the main volume of the erupted lava. Fast ascent of the foam hinders its crystallization and
975 preserves high number of vesicles, high vesicularity and it is only little modified by post-
976 fragmentation expansion. Decrease in initial overpressure translates in a progressive decrease
977 in magma ascent rate and output rate (e.g. Coppola et al., 2017 and references therein).
978 Nucleation of microcrysts is enhanced in melt ascending with lower speed and is mostly
979 related to syneruptive degassing (for the spiny).

980 The larger volume (dense lava) corresponds to crystallized and less vesiculated magma
981 which experiences a slow ascent in the dyke and even further micro-crystallisation during its
982 subaerial emplacement.

983 Melt inclusion results allow us to confirm the involvement of a single and only slightly
984 heterogeneous magma source in 2014, related to cooling and fractional crystallisation of an
985 older magma batch (November 2009). Interestingly, this latter short lived summit eruption
986 was also characterized by the same large textural range of pyroclastic products found in 2014
987 in spite of its more mafic composition.

988 This suggests that bubble accumulation and source pressurisation is highly dependent
989 on the shallow storage depth, which facilitates rapid water exsolution (Di Muro et al., 2016),

990 and it is not necessarily the outcome of slow magma cooling and differentiation (Tait et al.,
991 1989).

992 |

993 **6. Proposed model for the 2014 eruption and conclusions**

994 |

995 In this paper we show that textural and petro-chemical study of the eruptive products can be
996 used to characterize the on-going activity at PdF and to constrain both the trigger and the
997 evolution of short-lived and small-volume eruptions. This approach is extremely valuable in i)
998 understanding processes that lead to an eruption which was preceded by short-lived and
999 elusive precursors, and ii) in reconstructing the time evolution of eruptive dynamics in an
1000 eruption with poor direct observations.

1001 Following the sketch in Figure 12, we infer that residual magma from the 2009
1002 eruption ponding at shallow levels experienced long-lasting cooling and crystallization (Fig.
1003 12a). Between 2010 and 2014 the volcano progressively deflated (Fig. 12b) possibly because
1004 of magma degassing and cooling, facilitated by the shallow depth of the reservoir. During this
1005 phase mesocrysts and some microcrystallites formed (Figs. 4e and 10a).

1006 The occurrence of deep (>10 km bsl) lateral magma transfer since March-April 2014
1007 has been inferred by Boudoire et al., (2017) on the basis of deep (mantle level) seismic
1008 swarms and increase in soil CO₂ emissions on the distal western volcano flank. The incipit of
1009 magma transfer towards shallower crustal levels is potentially recorded by subtle volcano
1010 inflation about 11 days before the June 2014 eruptions (Figs. 1d and 12c). We suspect that
1011 these deep processes can have progressively modified the shallow crustal stress field and
1012 favoured magma vesiculation and melt-crystal separation. Second boiling could thus have
1013 over-pressured the shallow seated reservoir and triggered magma ascent (Fig. 12c).

1014 Without this deep magma transfers we believe that the small reservoir activated in
1015 2014 would have cooled down completely to form an intrusion (as suggested by the pervasive
1016 crystallization of the lava, one of the densest emitted from 2014 to 2017, [Harris et al. 2017](#)).
1017 The 2014 event represented instead the first of a long series of eruptions, whose magmas
1018 became progressively less evolved in time (Coppola et al., 2017). In this scenario the trigger
1019 mechanisms of 2014 activity are both internal and external in the sense that the small shallow
1020 reservoir hosting cooled magma permitted to create the conditions favourable to a second
1021 boiling (Fig. 12c, and Tait et al., 1989). The second boiling was likely triggered by an almost

1022 undetectable stress field change, and was favoured by the shallow storage pressure of the
1023 magma (Fig. 12c) that promoted fast water exsolution and rapid magma response to external
1024 triggers. The second boiling possibly contributed to the inflation registered 11 days before the
1025 eruption at 1.4-1.7 km (Fig. 12c) caused both by magma expansion and transfer of hot fluids
1026 to the hydrothermal system (Lénat et al., 2011).

1027 Our data permit to exclude (i) new magma input and/or fluid inputs (CO₂-rich fluids)
1028 from deep magmatic levels to trigger the June 2014 eruption. We also exclude (ii) heating and
1029 enhanced convection of the shallow magma reservoir (due to heat diffusion without fluid or
1030 mass transfer), because this process is very slow. Furthermore, the 2014 minerals do not
1031 record evidences of magma heating. We can exclude equally (iii) deformation of the volcanic
1032 edifice and decompression of the magma reservoir and/or hydrothermal system due to flank
1033 sliding because geodetic data show no evidence of flank sliding able to produce stress change
1034 in the hydrothermal and magmatic system. Geophysical and geochemical data have permitted
1035 to track vertical magma and fluid transfer below the volcano summit in April 2015, that is
1036 about one year after the early deep lateral magma transfer (Peltier et al., 2016). Deep
1037 processes are difficult to detect for any monitoring network.

1038 We conclude that the overpressure, caused by the second boiling, triggered the
1039 eruption. The occurrence of a hydrous almost pure melt at shallow depth permitted its fast
1040 vesiculation upon ascent towards the surface. In turn, fast ascent of the foam (Fig. 12d)
1041 hindered its crystallization and preserved high number of vesicles. Decrease in initial
1042 overpressure translated in a progressive decrease in magma ascent rate and output rate (e.g.
1043 Coppola et al., 2017 and references therein) and a temporal transition from Hawaiian activity
1044 to Strombolian activity (Fig. 12 d). Nucleation of microcrysts was enhanced in melt ascending
1045 with lower speed and in turn this syn-eruptive crystallization favoured bubble
1046 connectivity/permeability in the ascending magma, even for magma at low vesicularity. The
1047 largest volume (dense lava) corresponds to highly-crystallized and degassed magma already
1048 in the reservoir, that experienced a slower ascent in the dyke and even further micro-
1049 crystallisation during its subaerial emplacement.

1050 The texture of the products allowed us to follow the dynamic evolution of the system
1051 in space, from smooth fluidal scoria emitted from rapid jet of lava at the fractures, to a more
1052 stable activity at the MV, and in time. At the MV, in fact, we observed the transition from the
1053 golden and fluidal fragments emitted from Hawaiian fountaining, at the peak of the intensity
1054 of the eruption, to the spiny fragments, emitted from a declining Strombolian activity at the
1055 end of the eruption.

1056 Therefore we here show for the first time that short lived and weak Hawaiian
1057 fountaining and Strombolian events can preserve pyroclast textures that can be considered a
1058 valid approximation to [shallow reservoir conditions and ascent degassing processes](#) ~~magma~~
1059 ~~ascent and fragmentation conditions~~ before the explosions and correlate to the eruptive
1060 dynamics as well.

1061 To conclude, these results highlight the importance of petrological monitoring, which
1062 can provide complementary information regarding the ongoing volcanic activity to other
1063 geophysical and geochemical monitoring tools commonly used on volcanoes.

1064 **Acknowledgements**

1065 OVPF team and T. Lecocq for monitoring and fieldwork. F. van Wyk de Vries provided an
1066 English revision for the proof. We thank the STRAP project funded by the Agence Nationale
1067 de la Recherche (ANR-14-CE03-0004-04). This research was financed by the French
1068 Government Laboratory of Excellence initiative no. ANR-10-LABX-0006, the Région
1069 Auvergne, and the European Regional Development Fund. This is Laboratory of Excellence
1070 Clervolc contribution number XXXX

1071

1072 **References list**

1073 Albarède, F., and V. Tamagnan (1988), Modelling the recent geochemical evolution of the
1074 Piton de la Fournaise volcano, Réunion island, 1931-1986, *J. Petrol.*, 29, 997-1030.

1075 Albarède, F., B. Luais, G. Fitton, M.P. Semet, E. Kaminski, B.G.J Upton, P. Bachèlery, and
1076 J.L. Cheminée (1997), The geo-chemical regimes of Piton de la Fournaise Volcano Réunion.
1077 during the last 530,000 years, *J. Petrol.*, 38, 171–201.

1078 Andronico, D., M.D. Lo Castro, M. Sciotto, and L. Spina (2013a), The 2010 ash emissions at
1079 the summit craters of Mt Etna: relationship with seismo-acoustic signals, *J. Geophys. Res.*,
1080 118, 51–70, doi:10.1029/2012JB009895.

1081 Andronico, D., J. Taddeucci, A. Cristaldi, L. Miraglia, P. Scarlato, and M. Gaeta (2013b), The
1082 15 March 2007 paroxysm of Stromboli: video-image analysis, and textural and compositional
1083 features of the erupted deposit, *Bull. Volcanol.*, 75, 733, doi:10.1007/s00445-013-0733-2.

1084 Andronico, D., S. Scollo, M.D. Lo Castro, A. Cristaldi, L. Lodato, and J. Taddeucci (2014),
1085 Eruption dynamics and tephra dispersal from the 24 November 2006 paroxysm at South-East
1086 Crater, Mt Etna, Italy, *J. Volcanol. Geotherm. Res.*, 274, 78–91,
1087 doi:10.1016/j.jvolgeores.2014.01.009.

1088 Bachèlery, P., J.F. Lénat, A. Di Muro, and L. Michon (2016), Active Volcanoes of the
1089 Southwest Indian Ocean: Piton de la Fournaise and Karthala. Active Volcanoes of the World.
1090 Springer-Verlag, Berlin and Heidelberg, 1-428, DOI 10.1007/978-3-642-31395-0_12.

1091 Boivin, P., and P. Bachèlery (2009), Petrology of 1977 to 1998 eruptions of Piton de la
1092 Fournaise, La Réunion Island, *J. Volcanol. Geotherm. Res.*, 184, 109–125.

1093 Bombrun, M., A. Harris, L. Gurioli, J. Battaglia and V. Barra (2015), Anatomy of a
1094 strombolian eruption: inferences from particle data recorded with thermal video, *J. Geophys.*
1095 *Res.*, 120(4):2367-2387. DOI.10.1002/2014BO11556.

1096 Boudoire, G., M. Liuzzo, A. Di Muro, V. Ferrazzini, L. Michon, F. Grassa, A. Derrien, N.
1097 Villeneuve, A. Bourdeu, C. Brunet, G. Giudice, and S. Gurrieri (2017), Investigating the
1098 deepest part of a volcano plumbing system: evidence for an active magma path below the
1099 western flank of Piton de la Fournaise (La Réunion Island), *J. Volcanol. Geotherm. Res.*, doi:
1100 10.1016/j.jvolgeores.2017.05.026.

1101 Brenguier, F., P. Kowalski, T. Staudacher, V. Ferrazzini, F. Lauret, P. Boissier, A. Lemarchand,
1102 C. Pequegnat, O. Meric, C. Pardo, A. Peltier, S. Tait, N.M. Shapiro, M. Campillo, and A. Di
1103 Muro (2012), First Results from the UnderVolc High Resolution Seismic and GPS network
1104 deployed on Piton de la Fournaise Volcano, *Seismo. Res. Lett.* 83(7),
1105 doi:10.1785/gssrl.83.1.97.

1106 Brugier, Y.A. (2016), Magmatologie du Piton de la Fournaise (Ile de la Réunion): approche
1107 volcanologique, pétrologique et expérimentale. Sciences de la Terre. Université d'Orléans,
1108 NNT: 2016ORLE2007, pp. 251.

1109 Bureau, H., F. Pineau, N. Métrich, P.M. Semet, and M. Javoy (1998a), A melt and fluid
1110 inclusion study of the gas phase at Piton de la Fournaise volcano (Reunion Island), *Chem.*
1111 *Geol.* 147, 115–130.

1112 Bureau, H., N. Métrich, F. Pineau, and M.P. Semet (1998b), Magma-conduit interaction at
1113 Piton de la Fournaise volcano (Réunion Island): a melt and fluid inclusion study, *J. Volcanol.*
1114 *Geotherm. Res.* 84, 39–60.

1115 Carey, R.J., M. Manga, W. Degruyter, D. Swanson, B. Houghton, T. Orr, and M. Patrick
1116 (2012), Externally triggered renewed bubble nucleation in basaltic magma: the 12 October
1117 2008 eruption at Halema‘uma‘u Overlook vent, Kīlauea, Hawai‘i, USA, *J. Geophys. Res.*,
1118 117, B11202. doi:10.1029/2012JB009496.

1119 Carey, R.J., M. Manga, W. Degruyter, H. Gonnermann, D. Swanson D, B. Houghton, T. Orr,
1120 and M. Patrick (2013), Convection in a volcanic conduit recorded by bubbles, *Geology*, 41(4),
1121 395–398.

1122 Cashman, K.V., and M.T. Mangan (1994) Physical aspects of magmatic degassing II:
1123 constraints on vesiculation processes from textural studies of eruptive products, In: Carroll
1124 MR, Holloway JR (eds) Volatiles in magmas, Reviews in mineralogy. *Miner. Soc. Am.*,
1125 Fredricksberg, pp 447–478.

1126 Clocchiatti, R., A. Havette, and P. Nativel (1979), Relations pétrogénétiques entre les basaltes
1127 transitionnels et les océanites du Piton de la Fournaise (Ile de La Réunion, océan Indien) à
1128 partir e la composition chimique des inclusions vitreuses des olivines et des spinelles, *Bull.*
1129 *Minér.*, 102, 511–525.

1130 Colombier, M., L. Gurioli, T.H. Druitt, T. Shea, P. Boivin, D. Miallier, and N. Cluzel (2017a),
1131 Textural evolution of magma during the 9.4-ka trachytic explosive eruption at Kilian Volcano,
1132 Chaîne des Puys, France, *Bull. Volcanol.*, 79(2), 1-24. doi:10.1007/s00445-017-1099-7.

1133 Colombier, M., F.B. Wadsworth, L. Gurioli, B. Scheu, U. Kueppers, A. Di Muro, and D.B.
1134 Dingwel (2017b), The evolution of pore connectivity in volcanic rocks, *Earth Planet. Sci.*
1135 *Lett.*, 462, 99-109. DOI: 10.1016/j.epsl.2017.01.011.

1136 Colò, L., M. Ripepe, D.R. Baker, and M. Polacci (2010), Magma vesiculation and infrasonic
1137 activity at Stromboli open conduit volcano, *Earth Planet. Sc. Lett.* 292(3–4):274–280.

1138 Coppola, D., N. Villeneuve, A. Di Muro, V. Ferrazzini, A. Peltier, M. Favalli, P. Bachèlery, L.
1139 Gurioli, A. Harris, S. Moune, I. Vlastélic, B. Galle, S. Arellano, and A. Aiuppa (2017), A
1140 Shallow system rejuvenation and magma discharge trends at Piton de la Fournaise volcano
1141 (La Réunion Island), *Earth Planet. Sci. Lett.* 463, 13-24.

- 1142 Corsaro, R., and L. Miraglia (2014), The transition from summit to flank activity at Mt. Etna,
1143 Sicily (Italy): Inferences from the petrology of products erupted in 2007–2009, *J. Volcanol.*
1144 *Geother. Res.*, 275, 51–60.
- 1145 Darcy, H. (1856) Les Fontaines Publiques de la Ville de Dijon, Dalmont, Paris.
- 1146 Di Muro, A., Métrich, N., Vergani, D., Rosi, M., Armienti, P., Fougeroux, T., Deloule, E.,
1147 Arienzo, I., Civetta, L. (2014), The shallow plumbing system of Piton de la Fournaise Volcano
1148 (La Réunion Island, Indian Ocean) revealed by the major 2007 caldera forming eruption, *J.*
1149 *Petrol.*, 55, 1287-1315.
- 1150 Di Muro, A., T. Staudacher, V. Ferrazzini, N. Métrich, P. Besson, C. Garofalo, and B.
1151 Villemant (2015), Shallow magma storage at Piton de la Fournaise volcano after 2007 summit
1152 caldera collapse tracked in Pele’s hairs, chap 9 of Carey, R. J., V. Cayol, M. P. Poland, and D.
1153 Weis (eds.), Hawaiian Volcanoes: From Source to Surface, *American Geophysical Union*
1154 *Monograph 208*, pp 189–212, doi:10.1002/9781118872079.ch9.
- 1155 Di Muro, A., N. Métrich, P. Allard, A. Aiuppa, M. Burton, B. Galle, and T. Staudacher (2016),
1156 Magma degassing at Piton de la Fournaise volcano, Active Volcanoes of the World, series,
1157 Springer, Bachelery, P., Lenat, J.F, Di Muro, A., Michon L., Editors. Pg. 203-222.
- 1158 DYNVOLC Database (2017) Observatoire de Physique du Globe de Clermont-Ferrand,
1159 Aubière, France. DOI:10.25519/DYNVOLC-Database. Online access:
1160 <http://dx.doi.org/10.25519/DYNVOLC-Database>
- 1161 Eychenne, J., B.F. Houghton, D.A. Swanson, R.J. Carey, and L. Swavely (2015), Dynamics of
1162 an open basaltic magma system: the 2008 activity of the Halema’uma’u Overlook vent,
1163 Kīlauea Caldera. *Earth Planet. Sci. Lett.*, 409, 49–60.
- 1164 Famin, V., B. Welsch, S. Okumura, P. Bachèlery, and S. Nakashima (2009), Three
1165 differentiation stages of a single magma at Piton de la Fournaise (Réunion hotspot). *Geoch.*
1166 *Geoph. Geos.* 10, Q01007. doi:10. 1029/2008GC002015.
- 1167 Fisk, M.R., B.G.J Upton, C.E. Ford, and W.M. White (1988), Geochemical and experimental
1168 study of the genesis of magmas of Reunion island, Indian Ocean, *J. Geophys. Res.*, 93, 4933-
1169 4950.
- 1170 Forchheimer, P. (1901) Wasserbewegung durch Boden, *Z. Ver. Dtsch. Ing.* 45:1781–1788.

1171 Formenti, Y, and T.H. Druitt (2003), Vesicle connectivity in pyroclasts and implications for
1172 the fluidisation of fountain-collapse pyroclastic flows, Montserrat (West Indies), *Earth Planet.*
1173 *Sci. Lett.*, 214, 561–574.

1174 Gardner, J.E., R.M.E. Thomas, C. Jaupart, and S. Tait (1996), Fragmentation of magma
1175 during Plinian volcanic eruptions, *Bull. Volcanol.*, 58, 144–162.

1176 Giachetti, T., T.H. Druitt, A. Burgisser, L. Arbaret, and C. Galven (2010), Bubble nucleation
1177 and growth during the 1997 Vulcanian explosions of Soufrière Hills Volcano, Montserrat, *J.*
1178 *Volcanol. Geotherm. Res.*, 193(3–4):215–231. doi:10.1016/j.jvolgeores.2010.04.001.

1179 Gonnermann, H.M., and M. Manga (2013) Dynamics of magma ascent in the volcanic
1180 conduit. In: Fagents, S.A., Gregg, T.K.P., Lopes, R.M.C. (Eds.), *Modeling Volcanic Processes:*
1181 *The Physics and Mathematics of Volcanism.* Cambridge University Press, Cambridge.

1182 Gurioli, L., A.J.L. Harris, B.F. Houghton, M. Polacci, and M. Ripepe (2008) Textural and
1183 geophysical characterization of explosive basaltic activity at Villarrica volcano, *J. Geophys.*
1184 *Res.*, 113, B08206. doi:10.1029/2007JB005328

1185 Gurioli, L., A.J.L. Harris, L. Colo, J. Bernard, M. Favalli, M. Ripepe, and D. Andronico
1186 (2013), Classification, landing distribution and associated flight parameters for a bomb field
1187 emplaced during a single major explosion at Stromboli, Italy, *Geology*, 41, 559-562, DOI
1188 10.1130/G33967.1.

1189 Gurioli, L., L. Colo', A.J. Bolasina, A.J.L. Harris, A. Whittington, and M. Ripepe (2014),
1190 Dynamics of strombolian explosions: inferences from inferences from field and laboratory
1191 studies of erupted bombs from Stromboli volcano, *J. Geophys. Res.*, 119(1),
1192 DOI:10.1002/2013JB010355.

1193 Gurioli, L., D. Andronico, P. Bachelery, H. Balcone-Boissard, J. Battaglia, G. Boudon, A.
1194 Burgisser, S.B. M.R. Burton, K. Cashman, S. Cichy, R. Cioni, A. Di Muro, L. Dominguez, C.
1195 D’Oriano, T. Druitt, A.J.L Harris, M. Hort, K. Kelfoun, J.C. Komorowski, U. Kueppers, J.L.
1196 Le Penec, T. Menand, R. Paris, L. Pioli, M. Pistolesi, M. Polacci, M. Pompilio, M. Ripepe,
1197 O. Roche, E. Rose-Koga, A. Rust, L. Scharff, F. Schiavi, R. Sulpizio, J. Taddeucci, and T.
1198 Thordarson (2015), MeMoVolc consensual document: a review of cross-disciplinary
1199 approaches to characterizing small explosive magmatic eruptions, *Bull. Volcanol.*, 77, 49.
1200 DOI: 10.1007/s00445-015-0935-x.

1201 Hammer, J.E., K.V. Cashman, R.P. Hoblitt, and S. Newman (1999) Degassing and microlite
1202 crystallization during pre-climactic events of the 1991 eruption of Mt. Pinatubo, Philippines,
1203 *Bull. Volcanol.* 60, 355–380.

1204 Harris, A.J.L., N. Villeneuve, A. Di Muro, V. Ferrazzini, A. Peltier, D. Coppola, M. Favalli, P.
1205 Bachèlery, J.-L. Foger, L. Gurioli, S. Moune, I. Vlastélic, B. Galle, and S. Arellano (2017),
1206 Effusive Crises at Piton de la Fournaise 2014-2015: A Review of a Multi-National Response
1207 Model, *Applied Volcanology*, 6, 11, DOI 10.1186/s13617-017-0062-9

1208 Helz, R.T., and C.R. Thornber (1987), Geothermometry of Kilauea Iki lava lake, Hawaii, *Bull.*
1209 *Volcanol.*, 49, 651–668.

1210 Hibert, C, A. Mangeney, M. Polacci, A. Di Muro, S. Vergnolle, V. Ferrazzini, B. Taisne, M.
1211 Burton, T. Dewez, G. Grandjean, A. Dupont, T. Staudacher, F. Brenguier, N.M. Shapiro, P.
1212 Kowalski, P. Boissier, P. Catherine, and F. Lauret (2015), Multidisciplinary monitoring of the
1213 January 2010 eruption of Piton de la Fournaise volcano, La Réunion island, *J. Geophys. Res.*,
1214 120(5), 3026-3047

1215 Higgins M.-D. (2000). Measurement of crystal size distributions, *American Mineralogist*, 85,
1216 1105-1116.

1217 Houghton, B.F., and C.J.N. Wilson (1989), A vesicularity index for pyroclastic deposits, *Bull.*
1218 *Volcanol.*, 51, 451–462. doi:10.1007/BF01078811

1219 Houghton, B.F., D.A. Swanson, R.J. Carey, J Rausch., and A.J Sutton (2011), Pigeonholing
1220 pyroclasts, insights from the 19 March 2008 explosive eruption of Kīlauea volcano,
1221 *Geology*, 39, 263–266, doi:10.1130/G31509.1.

1222 Houghton, B.F., D.A. Swanson, J. Rausch, R.J. Carey, Fagents S.A., and T.R. Orr (2013),
1223 Pushing the volcanic explosivity index to its limit and beyond: constraints from exceptionally
1224 weak explosive eruptions at Kīlauea in 2008, *Geology*, 41(6):627–630

1225 Houghton, B.F., J. Taddeucci, D. Andronico, H.M. Gonnermann, M. Pistolesi, M.R. Patrick,
1226 T.R. Orr, D.A. Swanson, M. Edmonds, D. Gaudin, R.J. Carey and P. Scarlato (2016), Stronger
1227 or longer: Discriminating between Hawaiian and Strombolian eruption styles, *Geology* doi:
1228 10.1130/G37423.1

- 1229 Inman, D.L. (1952) Measures for describing the size distribution of sediments, *J. Sed. Petrol.*,
1230 22, 125–145.
- 1231 Kahl, M., S.Chakraborty, M. Pompilio, and F. Costa (2015), Constraints on the nature and
1232 evolution of the magma plumbing system of Mt. Etna Volcano (1991–2008) from a combined
1233 thermodynamic and kinetic modelling of the compositional record of minerals, *J.Petrol.*, 56,
1234 2025–2068, doi:10.1093/petrology/egv063.
- 1235 Kawabata, E., S.J. Cronin, M.S. Bebbington, M.R.H. Moufti, N. El-Masry, and T. Wang
1236 (2015), Identifying multiple eruption phases from a compound tephra blanket: an example of
1237 the AD1256 Al-Madinah eruption, Saudi Arabia, *Bull. Volcanol.*, 77, 6 DOI 10.1007/s00445-
1238 014-0890-y.
- 1239 Lange, R.A., H.M. Frey, and J. Hector (2009), A thermodynamic model for the plagioclase-
1240 liquid hygrometer/thermometer, *Am. Mineral.*, 94, 494–506.
- 1241 Lautze, N., J. Taddeucci, D. Andronico, C. Cannata, L. Tornetta, P. Scarlato, B. Houghton, and
1242 D. Lo Castro (2012), SEM-based methods for the analysis of basaltic ash from weak
1243 explosive activity at Etna in 2006 and the 2007 eruptive crisis at Stromboli, *Phys. Chem.*
1244 *Earth* 45,46, 113–127, doi:10.1016/j.pce.2011.02.001.
- 1245 Leduc, L., L. Gurioli, A.J.L. Harris, L. Colo', and E. Rose-Koga (2015), Types and
1246 mechanisms of strombolian explosions: characterization of a gas-dominated explosion at
1247 Stromboli, *Bull. Volcanol.*, 77, 8, DOI: 10.1007/s00445-014-0888-5
- 1248 Lénat, J.-F., P. Bachèlery, and A. Peltier (2011), The interplay between collapse structures,
1249 hydrothermal systems and magma intrusions: the case of the central area of Piton de la
1250 Fournaise volcano, *Bull. Volc.* doi:10.1007/s00445-011-0535-3
- 1251 Lénat, E.F., P.B. Bachelery, and O. Merle (2012), Anatomy of Piton de la Fournaise volcano
1252 (La Réunion, Indian Ocean), *Bull. Volcanol.* 74, 1945–1961.
- 1253 Lengliné, O, Z. Duputel, and V. Ferrazzini (2016), Uncovering the hidden signature of a
1254 magmatic recharge at Piton de la Fournaise volcano using small earthquakes, *Geophys. Res.*
1255 *Let.*, 43, doi: 10.1002/2016GL068383

- 1256 Lindoo, A., J.F. Larsen, K.V. Cashman, A.L. Dunn, and O.K Neill (2016), An experimental
1257 study of permeability development as a function of crystal-free melt viscosity, *Earth Planet.*
1258 *Sci. Lett.*, 435, 45–54, doi: 10.1016/j.epsl.2015.11.035.
- 1259 Lindoo, A., J.F. Larsen, K.V. Cashman, and J. Oppenheimer (2017), Crystal controls on
1260 permeability development and degassing in basaltic andesite magma, *Geology*, 45(9), p. 831-
1261 834.
- 1262 Liuzzo, M., Di Muro, A., Giudice, G., Michon, L., Ferrazzini, V., and Gurrieri, S. (2015),
1263 New evidence of CO₂ degassing anomalies on the Piton de la Fournaise volcano and the link
1264 with volcano tectonic structures *Geochemistry, Geophysics, Geosystems*, 16, doi:10.1002/
1265 2015GC006032.
- 1266 Mangan, M.T., and K.V. Cashman (1996), The structure of basaltic scoria and reticulite and
1267 inferences for vesiculation, foam formation, and fragmentation in lava fountains. *J. Volcanol.*
1268 *Geotherm. Res.*, 73, 1–18.
- 1269 Menand, T., and J.C. Phillips (2007), Gas segregation in dykes and sills. *J. Volcanol. Geother.*
1270 *Res.*, 159(4), 393–408. <https://doi.org/10.1016/j.jvolgeores.2006.08.003>.
- 1271 Michon, L., A. Di Muro, N. Villeneuve, C. Saint-Marc, P. Fadda, and F. Manta (2013),
1272 Explosive activity of the summit cone of Piton de la Fournaise volcano (La Réunion Island): a
1273 historical and geological review, *J. Volcanol. Geotherm. Res.* 263, 117-133.
- 1274 Moitra, P., H.M. Gonnermann, B.F. Houghton, and T. Giachetti (2013), Relating vesicle
1275 shapes in pyroclasts to eruption styles, *Bull. Volcanol.* 75, 691. doi:10.1007/s00445-013-0691-
1276 8
- 1277 Morgan D.J., and D.A. Jerram (2006), On estimating crystal shape for crystal size distribution
1278 analysis, *J. Volc. Geotherm. Res.*, 154, 1–7.
- 1279 Moune, S., O. Sigmarsson, P. Schiano, T. Thordarson, and J.K. Keiding (2012), Melt
1280 inclusion constraints on the magma source of Eyjafjallajökull 2010 flank eruption, *J.*
1281 *Geophys. Res.*, 117, B00C07, doi:10.1029/2011jb008718.
- 1282 Morandi, A., C. Principe, A. Di Muro, G. Leroi, L. Michon, and P. Bachèlery (2016), Pre-
1283 historic explosive activity at Piton de la Fournaise volcano. In: Bachèlery P, Lénat JF, Di
1284 Muro A, Michon L (eds) *Active Volcanoes of the Southwest Indian Ocean: Piton de la*

- 1285 Fournaise and Karthala. Active Volcanoes of the World. Springer-Verlag, Berlin and
1286 Heidelberg, pp 107–138
- 1287 Óladóttir, B., O. Sigmarsson, G. Larsen, and J.-L. Devidal (2011), Provenance of basaltic
1288 tephra from Vatnajökull subglacial volcanoes, Iceland, as determined by major- and trace-
1289 element analyses, *Holocene*, 21, 1037–1048, doi:10.1177/0959683611400456.
- 1290 Oppenheimer, J., A.C. Rust, K.V. Cashman, and B. Sandnes (2015), Gas migration regimes
1291 and outgassing in particle-rich suspensions, *Frontiers in Physics*, 3, 1–13, doi: 10 .3389 /fphy
1292 .2015 .00060.
- 1293 Ort, M.H., A. Di Muro, L. Michon, and P. Bachèlery (2016), Explosive eruptions from the
1294 interaction of magmatic and hydrothermal systems during flank extension: the Bellecombe
1295 Tephra of Piton de La Fournaise (La Réunion Island), *Bull. Volcanol.* 78, 5,
1296 doi:10.1007/s00445-015-0998-8.
- 1297 Papale P., R. Moretti, and D. Barbato (2006), The compositional dependence of the saturation
1298 surface of H₂O + CO₂ fluids in silicate melts, *Chemical Geology*, 229, 1/3, 78-95,
1299 doi:10.1016/j.chemgeo.2006.01.013.
- 1300 Parcheta, C.E., B.F. Houghton, and D.A. Swanson (2013), Contrasting patterns of vesiculation
1301 in low, intermediate, and high Hawaiian fountains: a case study of the 1969 Mauna Ulu
1302 eruption, *J. Volcanol. Geotherm. Res.*, 255, 79–89
- 1303 Peltier, A., P. Bachèlery, and T. Staudacher (2009), Magma transport and storage at Piton de la
1304 Fournaise (La Réunion) between 1972 and 2007: A review of geophysical and geochemical
1305 data. *J. Volcanol. Geotherm. Res.*, 184, 93-108.
- 1306 Peltier, A., F. Beauducel, N. Villeneuve, V. Ferrazzini, A. Di Muro, A. Aiuppa, A. Derrien, K.
1307 Jourde, and B. Taisne (2016), Deep fluid transfer evidenced by surface deformation during the
1308 2014–2015 unrest at Piton de la Fournaise volcano, *J. Volcanol. Geotherm. Res.*, 321, 140–
1309 148. <http://dx.doi.org/10.1016/j.jvolgeores.2016.04.031>.
- 1310 Polacci, M., R. Corsaro, and D. Andronico (2006), Coupled textural and compositional
1311 characterization of basaltic scoria: insights into the transition from Strombolian to fire
1312 fountain activity at Mount Etna, Italy, *Geology*, 34(3), 201–204. doi:10.1130/G223181.1.

- 1313 Polacci, M., C. Bouvet de Maisonneuve, D. Giordano, M. Piochi, L. Mancini L., W.
1314 Degruyter, and O. Bachmann (2014), Permeability measurements of Campi Flegrei
1315 pyroclastic products: an example from the Campanian Ignimbrite and Monte Nuovo
1316 eruptions. *J. Volcanol. Geotherm. Res.* 272, 16–22.
- 1317 Putirka, K.D. (2008), Thermometers and barometers for volcanic systems, *Rev. Mineral.*
1318 *Geochem.* 69, 61-120.
- 1319 Reynolds, O. (1900) Papers on Mechanical and Physical Subjects, Cambridge University
1320 Press.
- 1321 Roeder, P., E. Goffin, and C. Thornber (2006), Cotectic proportions of olivine and spinel in
1322 olivine-tholeiitic basalt and evaluation of pre-eruptive processes, *J. Petrol.*, 47, 883-900.
- 1323 Roult, G., A. Peltier, T. Staudacher, V. Ferrazzini, B. Taisne, A. Di Muro, and The OVPF
1324 Team (2012), A comprehensive classification of the Piton de la Fournaise eruptions (La
1325 Réunion Island) spanning the 1986–2010 period. Search for eruption precursors from the
1326 broad-band GEOSCOPE RER station analysis and interpretation in terms of volcanic
1327 processes, *J. Volcanol. Geotherm. Res.*, 241, 78–104.
- 1328 Rust, A.C., and K.V. Cashman (2011), Permeability controls on expansion and size
1329 distributions of pyroclasts, *J. Geophys. Res.*, 116, B11202.
- 1330 Saar, M.O., M. Manga, K.V. Cashman, and S. Fremouw (2001) Numerical models of the
1331 onset of yield strength in crystal-melt suspensions: *Earth Planet. Sci. Lett.*, 187, 367–379, doi:
1332 10.1016/S0012-821X(01)00289-8.
- 1333 Salaün, A., Villemant, B., Semet, M.P., and T. Staudacher (2010), Cannibalism of olivine-rich
1334 cumulate xenoliths during the 1998 eruption of Piton de la Fournaise (La Réunion hotspot):
1335 Implications for the generation of magma diversity. *J. Volcanol. Geotherm. Res.*, 198, 187-204.
- 1336 Schiano, P., K. David, I. Vlastélic, A. Gannoun, M. Klein, F. Nauret, and Bonnand P. (2012),
1337 Osmium isotope systematics of historical lavas from Piton de la Fournaise (Réunion Island,
1338 Indian Ocean), *Contrib. Mineral. Petrol.*, <http://dx.doi.org/10.1007/s00410-012-0774-0>.
- 1339 Shea, T., (2017) Bubble nucleation in magmas: a dominantly heterogeneous process? *J.*
1340 *Volcanol. Geotherm. Res.* 343, 155–170.

- 1341 Shea, T., B.F. Houghton, L. Gurioli, K.V. Cashman, J.E. Hammer, and B. Hobden (2010),
1342 Textural studies of vesicles in volcanic rocks: an integrated methodology, *J. Volcanol.*
1343 *Geotherm. Res.*, 190, 271–289.
- 1344 Shea, T., L. Gurioli, and B.F. Houghton (2012), Transitions between fall phases and
1345 pyroclastic density currents during the AD 79 eruption at Vesuvius: building a transient
1346 conduit model from the textural and volatile record, *Bull. Volcanol.*, 74, 2363–2381,
1347 doi:10.1007/s00445-012-0668-z.
- 1348 Sparks, R.S.J. (1978), The dynamics of bubble formation and growth in magmas: a review
1349 and analysis, *J. Volcanol. Geotherm. Res.*, 3, 1–37.
- 1350 Sparks, R.S.J. (2003). Forecasting volcanic eruptions, *Earth Planet. Sci. Lett.*, 210, 1–15.
- 1351 Spina, L., C. Cimarelli, B. Scheu, D. Di Genova, and D. B. Dingwell (2016) On the slow
1352 decompressive response of volatile- and crystal-bearing magmas: An analogue experimental
1353 investigation, *Earth Planet. Sci. Lett.*, 433, 44–53.
- 1354 Staudacher, T., and A. Peltier (2015), Ground deformation at Piton de la Fournaise (La
1355 Réunion Island), a review from 20 years of GNSS monitoring, In: Bachèlery P, Lénat, JF, Di
1356 Muro A, Michon L (ed) Active volcanoes of the Southwest Indian Ocean: Piton de la
1357 Fournaise and Karthala. Active volcanoes of the world. Springer, Berlin, 139–170.
1358 doi:10.1007/978-3-642-31395-0_9
- 1359 Staudacher, T., V. Ferrazzini, A. Peltier, P. Kowalski, P. Boissier, P. Catherine, F. Lauret, and
1360 F. Massin (2009), The April 2007 eruption and the Dolomieu crater collapse, two major
1361 events at Piton de la Fournaise (La Réunion Island, Indian Ocean). *J. Volcanol. Geother. Res.*
1362 184, 126–137, doi:10.1016/j.jvolgeores.2008.11.005.
- 1363 Stovall, W.K., B.F. Houghton, H.M. Gonnermann, S.A. Fagents, and D.A. Swanson (2011),
1364 Eruption dynamics of Hawaiian-style fountains: the case study of episode 1 of the Kīlauea Iki
1365 1959 eruption, *Bull. Volcanol.* 73, 511–529. doi:10.1007/s00445-010-0426-z.
- 1366 Stovall, W.K., B.F. Houghton, J.E. Hammer, S.A. Fagents, and D.A. Swanson (2012),
1367 Vesiculation of high fountaining Hawaiian eruptions: episodes 15 and 16 of 1959 Kīlauea Iki,
1368 *Bull. Volcanol.*, 74, 441–455, doi:10.1007/s00445-011-0531-7.

1369 Swanson, D.A., K. Wooten, and T. Orr (2009), Buckets of ash track tephra flux from
1370 Halema'uma'u crater, Hawai'i. *Eos Trans. AGU*, 90, 427–428. doi:10.1029/2009EO460003.

1371 Taddeucci, J., M. Pompilio, and P. Scarlato (2002), Monitoring the explosive activity of the
1372 July–August 2001 eruption of Mt. Etna (Italy) by ash characterization, *Geophys. Res. Lett.*,
1373 29(8), 1029–1032. doi:10. 1029/2001GL014372.

1374 Tait, S., C. Jaupart, and S. Vergnolle (1989), Pressure, gas content and eruption periodicity of
1375 a shallow, crystallising magma chamber, *Earth Planet. Sci. Lett.*, 92, 107-123.

1376 Takeuchi, S., S. Nakashima, and A. Akihiko Tomiya (2008) Permeability measurements of
1377 natural and experimental volcanic materials with a simple permeameter: toward an
1378 understanding of magmatic degassing processes, *J. Volcanol. Geotherm. Res.*, 177:329–339.

1379 Thornber, C.R., K. Hon, C. Heliker, and D.A. Sherrod (2003), A Compilation of Whole-Rock
1380 and Glass Major-Element geochemistry of Kīlauea Volcano, Hawai'i, near-vent eruptive
1381 products: January 1983 through September 2001: *U.S.G.S. Open File Report*, 03-477.

1382 Thordarson, T, S Self, N Óskarsson, and T Hulsebosch (1996), Sulfur, chlorine and fluorine
1383 degassing and atmospheric loading by the 1783–1784 AD Laki (Skaftár Fires) eruption in
1384 Iceland, *Bull. Volcanol.* 58, 205–225.

1385 Villemant, B., A. Salaün, and T. Staudacher (2009), Evidence for a homogeneous primary
1386 magma at Piton de la Fournaise (La Réunion): A geochemical study of matrix glass, melt
1387 inclusions and Pélé's hairs of the 1998–2008 eruptive activity, *J. Volcanol. Geotherm. Res.*,
1388 184, 79–92.

1389 Vlastélic, I., and A.J. Pietruszka (2016), A review of the recent geochemical evolution of
1390 Piton de la Fournaise Volcano (1927–2010). In: Bachèlery, P., Lénat, J.F., Di Muro, A.,
1391 Michon, L. (Eds.), Active Volcanoes of the Southwest Indian Ocean. In: Active Volcanoes of
1392 the World, pp.185–201.

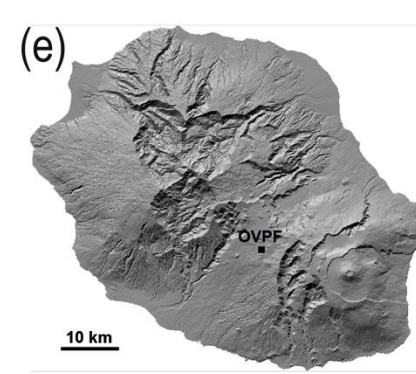
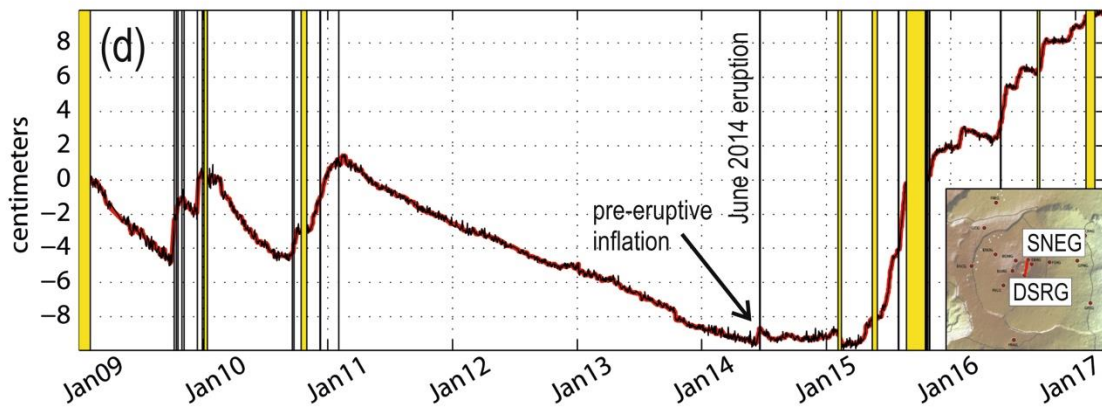
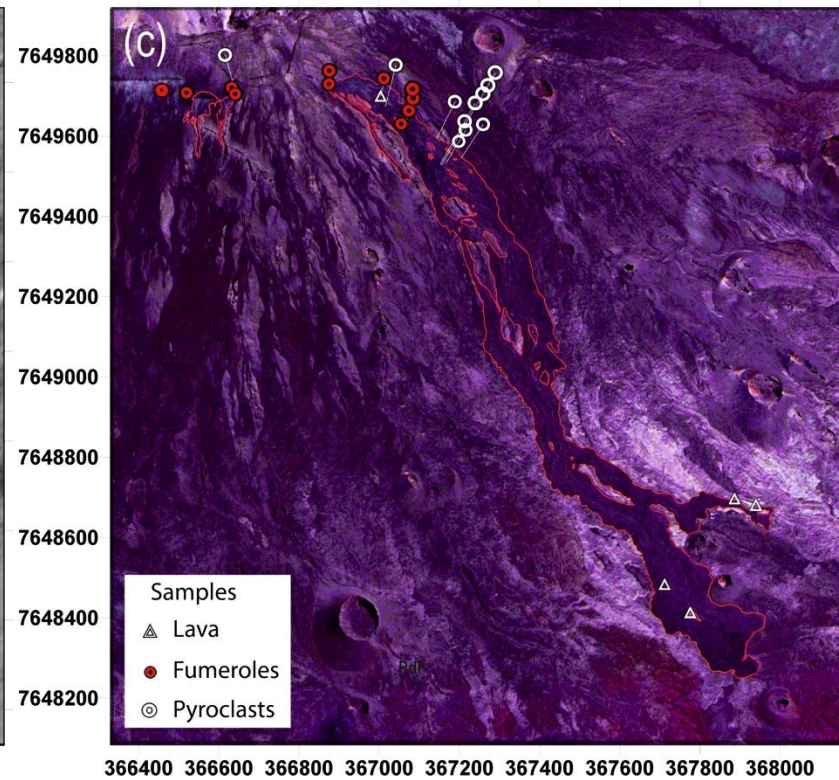
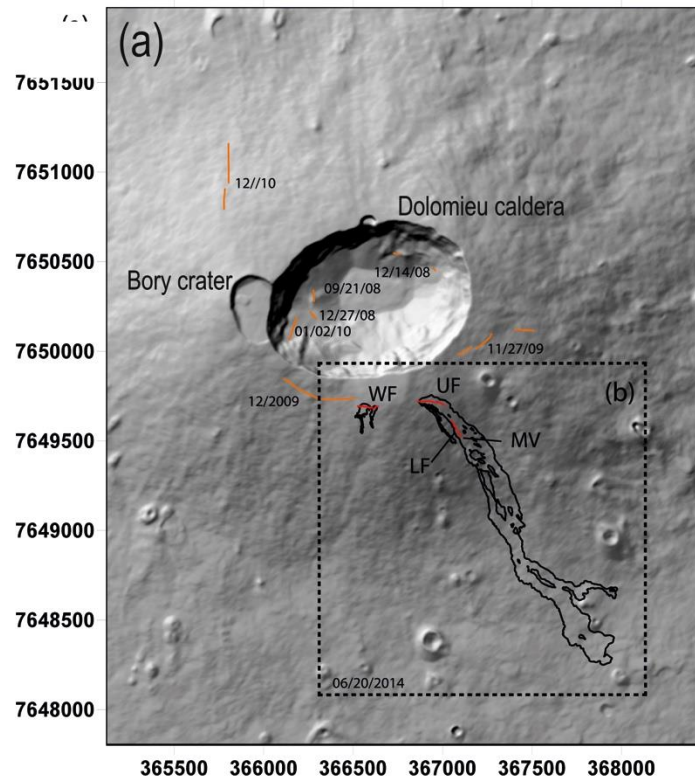
1393 Vlastélic, I., A. Peltier, and T. Staudacher (2007), Short-term (1998-2006) fluctuations of Pb
1394 isotopes at Piton de la Fournaise volcano (Réunion Island): origins and constraints on the size
1395 and shape of the magma reservoir, *Chem. Geology*, 244, 202-220.

1396 Vlastélic, I., C. Deniel, C. Bosq, P. Telouk, P. Boivin, P. Bachèlery, V. Famin,. and T.
1397 Staudacher (2009), Pb isotope geochemistry of Piton de la Fournaise historical lavas, *J.*
1398 *Volcanol. Geother. Res.*, 184, 63-78.

- 1399 Vlastélic, I., T. Staudacher, P. Bachèlery, P. Télouk, D. Neuville., and M. Benbakkar (2011)
1400 Lithium isotope fractionation during magma degassing: constraints from silicic differentiates
1401 and natural gas condensates from Piton de la Fournaise volcano (Réunion Island), *Chemical*
1402 *Geology*, 284, 26–34.
- 1403 Vlastélic, I., G. Menard, M. Gannoun, J.-L. Piro., T. Staudacher, and V. Famin (2013), Magma
1404 degassing during the April 2007 collapse of Piton de la Fournaise: the record of semi-volatile
1405 trace elements (Li, B, Cu, In, Sn, Cd, Re, Tl, Bi), *J. Volcanol. Geother. Res.*, 254, 94-107.
- 1406 Vlastélic, I., A. Gannoun, A. Di Muro, L. Gurioli, P. Bachèlery, and J.M. Henot (2016), Origin
1407 and fate of sulfide liquids in hotspot volcanism (La Réunion): Pb isotope constraints from
1408 residual Fe–Cu oxides, *Geochim. Cosmochim. Acta*, 194, 179-192.
- 1409 Welsch, B., F. Faure, P. Bachèlery, and V. Famin (2009), Microcrysts record transient
1410 convection at Piton de la Fournaise volcano (La Réunion Hotspot), *J. Petrol.*, 50, 2287-2305.
- 1411 Welsch, B., V. Famin, A. Baronnet, and P. Bachèlery (2013), Dendritic crystallization: a single
1412 process for all textures of olivine in basalts? *J. Petrol.*, 54, 539-574.
- 1413 White, J.D.L., and B.F. Houghton (2006), Primary volcanoclastic rocks, *Geology*, 34, 677–
1414 680, doi:10.1130/G22346.1.

1415 | [Figure captions](#)

1416



1417

1418 **Figure 1** a) Digital elevation model of the summit crater area at Piton de la Fournaise, La Réunion, France; orange = fractures generated by pre-
1419 2014 eruptions (reported are the dates of their activities); b) red = fractures active during the 2014 eruption: WF (Western Fracture), UF (Upper
1420 Fracture), LF (Lower Fracture), MV (Main Vent). Black= outline of the 2014 lava field; c) locations of sample collection points. The coordinates
1421 | are in UTM, zone 40 sSouth. (d) Distance change (baseline) in centimetres between two GNSS summit stations: DSRG and SNEG (see location
1422 | in the inset). Increase and decrease of the signal mean a summit inflation and deflation, respectively. The yellow areas represent eruptive and
1423 | intrusive periods. In Ffigure 1d, the rapid and strong variations linked to dike injections preceding intrusions and eruptions by a few tens of
1424 minutes have been removed; (e) Digital Elevation Model of La Réunion island.

1425

1426

June 2014 eruption at PdF

Early morning, June 21



June 21 ~ 7h00



June 21, 7h38

June 21, 13h35



June 21, 17h00



1427

1428 **Figure 2** Photos collection from the 2014 eruption at the MV, highlighted with a white cross
1429 (see location in Fig. 1). From a to g: evolution of the Strombolian activity from early morning
1430 to evening, June 21 that shows a decline in the activity with time. Unfortunately, the relatively
1431 more energetic Hawaiian fountaining events that happened during the night were not
1432 documented. a) Strombolian activity at the MV and associated lava flow; b) zoom view of the
1433 Strombolian activity at the MV. The images in a, b and the inset in b are from Laurent Perrier;
1434 c) aerial view of the SE flank of the PdF, taken by the OVPF team from the helicopter of the
1435 gendarmerie of La Réunion; d) Eastern front of the lava where the OVPF team collected a
1436 quenched lava sample; e) low Strombolian activity at the MV and the associated lava flow,
1437 photo from: [http://www.ipreunion.com/volcan/reportage/2014/06/21/eruption-du-piton-de-la-](http://www.ipreunion.com/volcan/reportage/2014/06/21/eruption-du-piton-de-la-fournaise-actualise-a-17h-la-lave-coule-sur-1-5-kilometre,26023.html)
1438 [fournaise-actualise-a-17h-la-lave-coule-sur-1-5-kilometre,26023.html](http://www.ipreunion.com/volcan/reportage/2014/06/21/eruption-du-piton-de-la-fournaise-actualise-a-17h-la-lave-coule-sur-1-5-kilometre,26023.html); f) and g) decline of the
1439 Strombolian activity at the MV, the photo in e) is from [http://www.zinfos974.com/L-](http://www.zinfos974.com/L-eruption-du-Piton-de-la-Fournaise-Le-point-de)
1440 [eruption-du-Piton-de-la-Fournaise-Le-point-de](http://www.zinfos974.com/L-eruption-du-Piton-de-la-Fournaise-Le-point-de) 17h_a72981.html; and the photo if f) is from:
1441 f) <http://nancyroc.com/eruption-a-la-reunion>

1442

1443

1444

1445

1446

1447

1448

1449

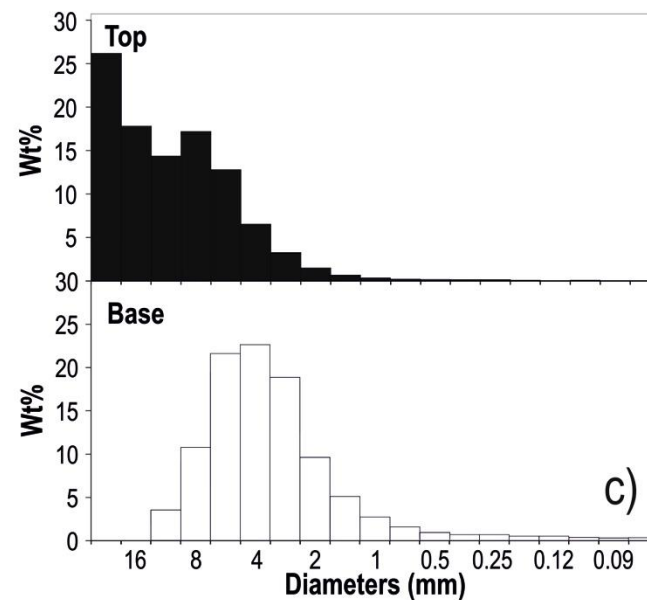
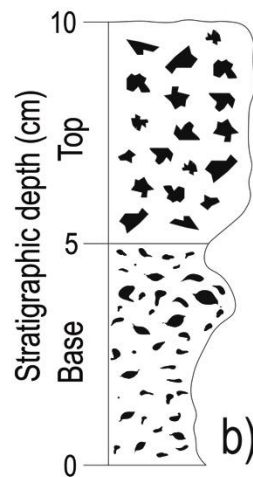
1450

1451

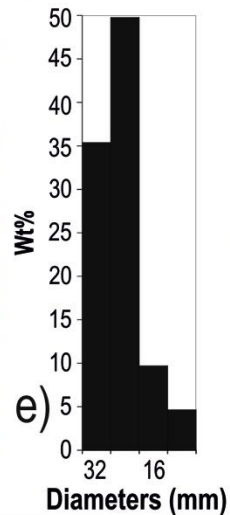
1452

1453

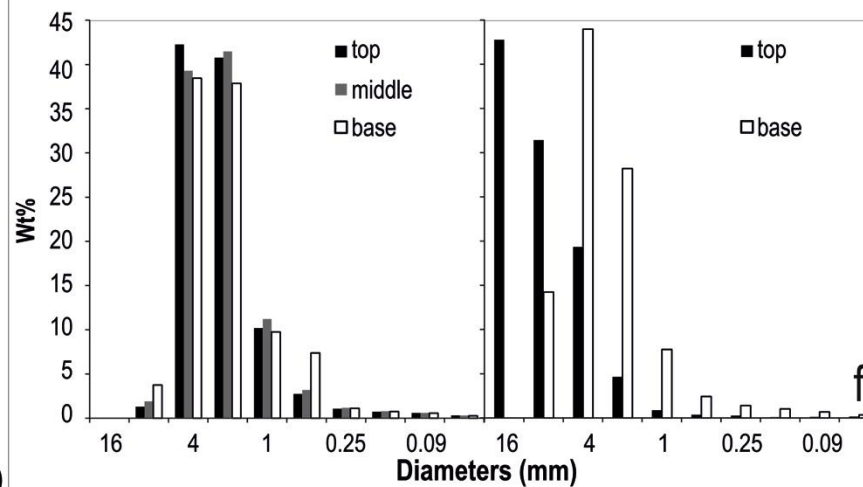
Main Vent



Western fracture



2010 Fountaining 2014 Explosions



1455 **Figure 3** a) Continuous blanket of scoria fall out deposit emitted from the MV (Fig. 1 for location) during June 2014 eruption at PdF. The black
1456 cross locates the position of the MV (see Fig. 1 for the location); b) schematic stratigraphic log of the scoria fall out deposit emplaced during
1457 June 2014 eruption at the MV. c) grain size histograms of the base and the top of the deposit of the MV, the particle diameters are at half phi; d)
1458 scattered scoria (outlined in yellow) from the WF (see Fig. 1 for the location); e) grain size histogram of the scoria deposit at the WF, the particle
1459 diameters are at half phi; f) comparison between the grain size histograms for the 2010 Hawaiian fountaining and the 2014 MV activity, both the
1460 particle axes are reported in full phi for comparison.

1461

1462

1463

1464

1465

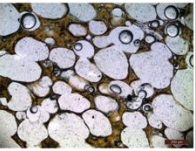
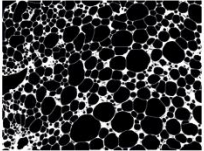
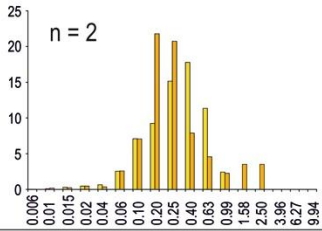
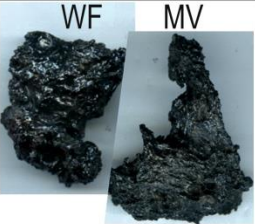
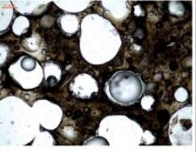
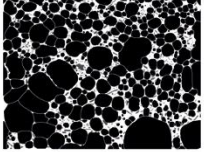
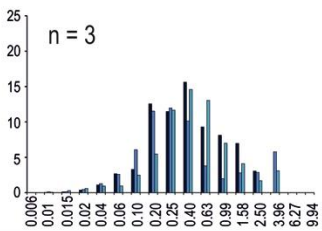
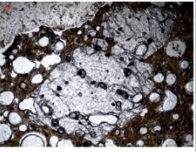
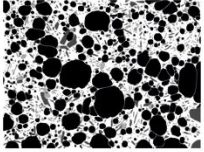
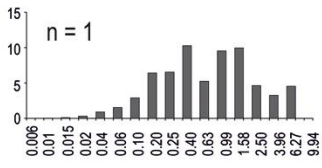
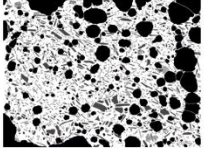
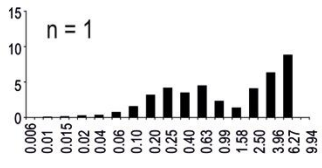
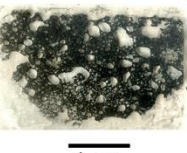
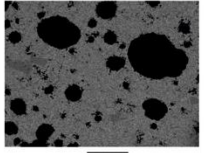
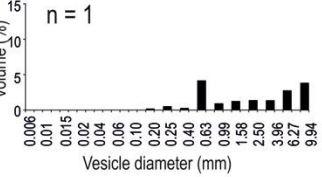
1466

1467

1468

1469

1470

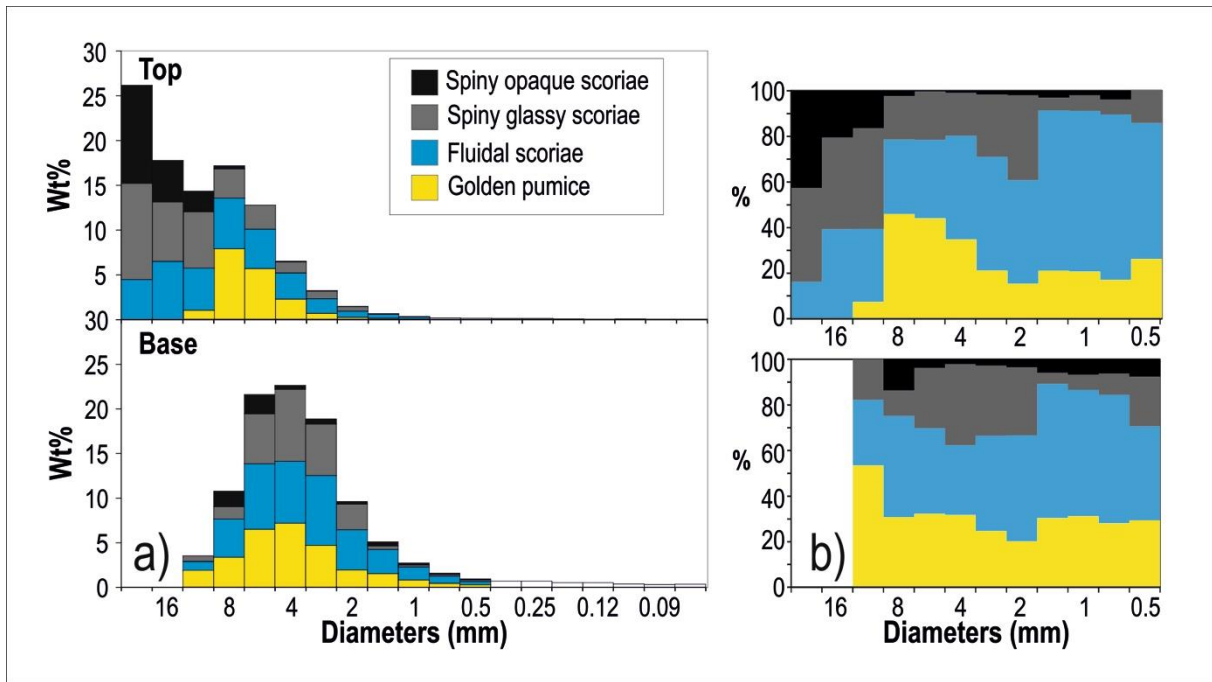
| Type | Clast | Thin section | Microscope | SEM (25X) | VSD | Crystal vol % | N_v |
|----------------------------|---|---|--|--|--|---|---|
| Golden Pumice (a) |  |  |  0.02 mm |  |  n = 2 | Tot = 8-15 Mplg = rare μ plg = 6-11 Mcpx = rare μ cpx = (1-3) | 2×10^7 9×10^6 |
| Fluidal Scoria (b) |  |  |  0.02 mm |  |  n = 3 | Tot = 4-23 Mplg = 0.4-1 μ plg = 2-19 Mcpx = 0-1 μ cpx = 1-4 | 2×10^7 5×10^6 3×10^6 |
| Spiny glassy scoria (c) |  |  |  0.02 mm |  |  n = 1 | Tot = 51 Mplg = 11 μ plg = 23 Mcpx = 15 μ cpx = 2 | 6×10^6 |
| Spiny opaque scoria (d) |  1 cm |  |  0.02 mm |  |  n = 1 | Tot = 55 Mplg = 11 μ plg = 25 Mcpx = 10 μ cpx = 9 | 4×10^6 |
| Lava (e) |  1 m |  1 cm |  0.02 mm |  1 mm |  n = 1 | Tot = 100 Mplg = 2 μ plg = 64 Mcpx = 3 μ cpx = 31 | 2×10^4 |

1472 **Figure 4** Textural features of June 2014 pyroclasts and lava. Clast = photo of the different types of juvenile pyroclasts and lava channel. The
1473 photo of the lava channel is from Laurent Perrier. WF = Western Fracture (smooth fluidal scoria), MV = Main Vent (fluidal scoria, less smooth
1474 than the ones at the WF). Thin section = thin section imaged with a desktop scanner. Microscope = picture taken with an optical microscope
1475 using natural light; SEM (25X) = image captured using a scanning electron microscopy (SEM), in BSE mode at 25x magnification: black are
1476 vesicles, white is glass, grey are crystals. VSD = vesicle ~~volume~~-size distribution histograms, where the diameter, in mm, is plotted versus the
1477 volume percentage, n = number of measured clasts; Crystal vol. % : Tot = total percentage of crystals corrected for the vesicularity; Mplg =
1478 percentage of mesocrysts of plagioclase; μ plg = percentage of microcrysts of plagioclase; Mcpx = percentage of mesocrysts of pyroxene; μ cpx =
1479 percentage of microcrysts of pyroxene; Nv = number density corrected for the vesicularity.

1480

1481

1482



1483

1484 **Figure 5** Proportion of each type of clast measured from the base to the top of the 10 cm thick
1485 deposit emplaced during the eruption, at the MV site. The deposit is dominated by Hawaiian-
1486 like lapilli fragments at the base (golden pumice and fluidal scoria) and Strombolian-like
1487 bombs and lapilli at the top (spiny scoria): (a) componentry within the different grain size
1488 classes; b) normalized componentry composition from the base to the top of the deposit.

1489

1490

1491

1492

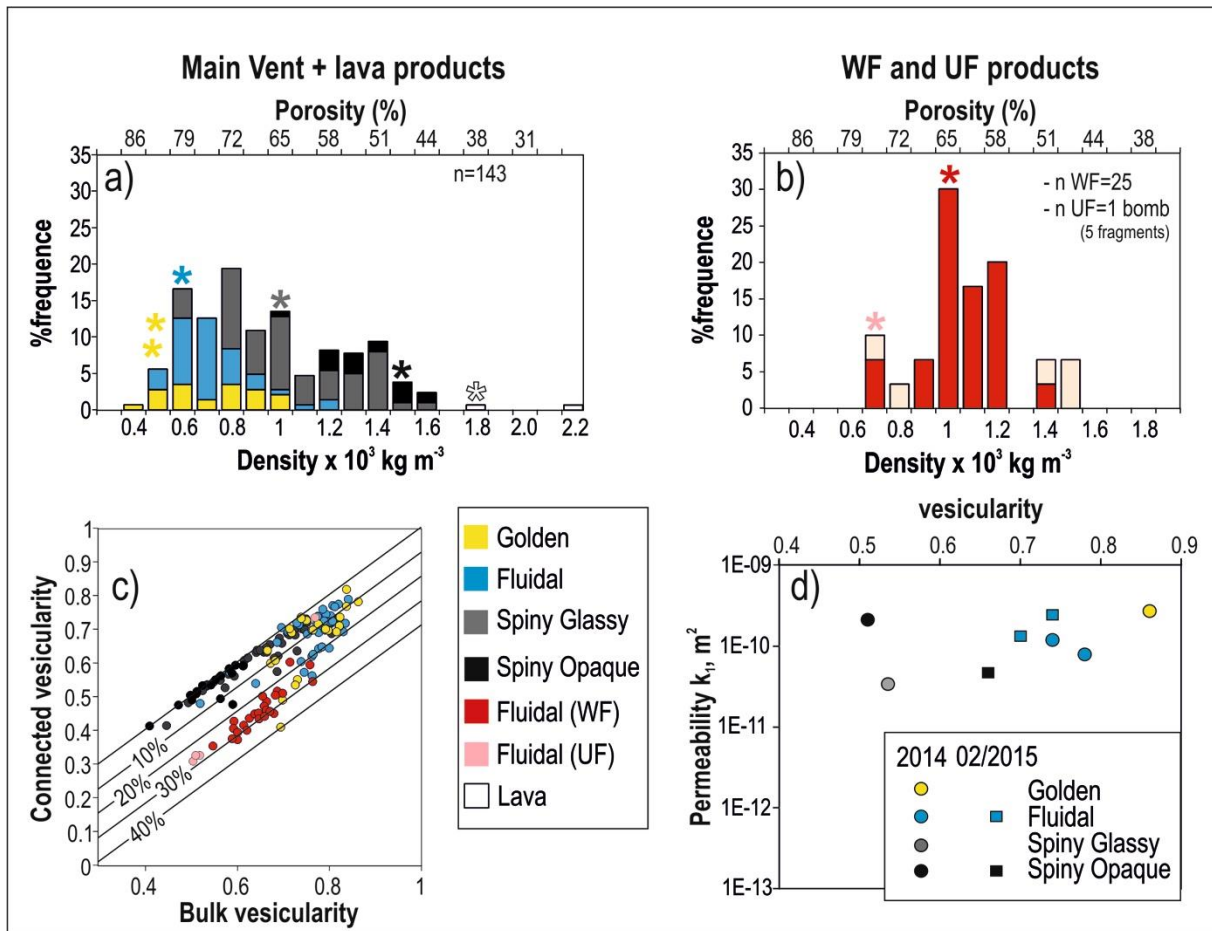
1493

1494

1495

1496

1497

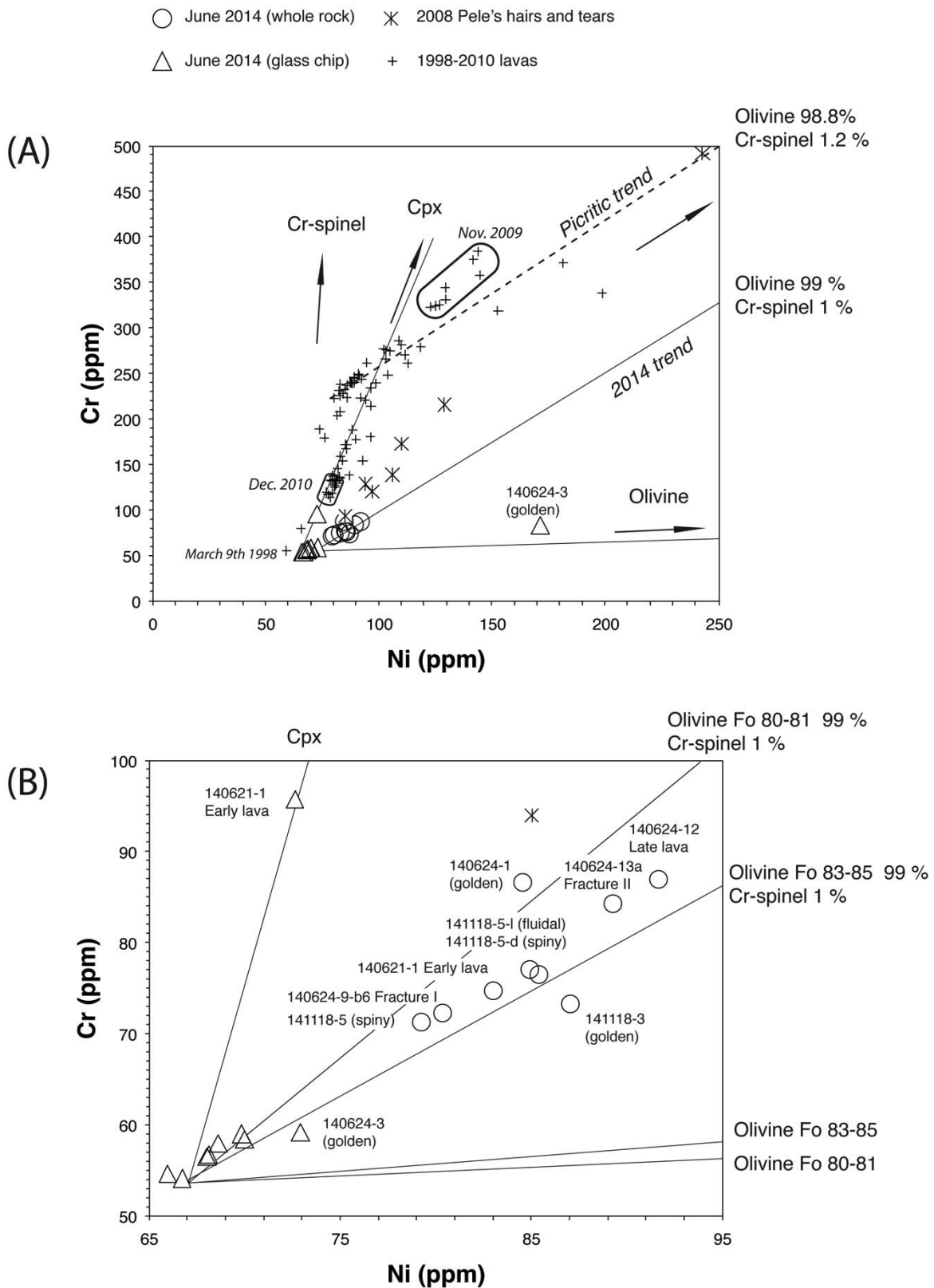


1498

1499 **Figure 6** Density, connectivity and permeability data of June 2014 pyroclast and lava
 1500 fragments: a) density distribution histogram for all the pyroclast fragments measured at the
 1501 MV + two lava fragments collected from the Eastern front of the lava flow (see Fig. 1 for
 1502 location). n = number of measured clasts; b) density distribution histogram for the pyroclasts
 1503 sampled at the WF and the bomb sampled at the UF. The bomb broke in five fragments (2
 1504 fragments from the core, the least dense, and three fragments from the quenched edges, the
 1505 densest). ~~and c)~~ In both the density histograms the stars represent the density intervals from
 1506 which we picked the clasts for the textural measurements; c) graph of the connected
 1507 vesicularity versus total vesicularity. The diagonal line represents equality between the
 1508 connectivity and vesicularity, beneath this line the samples have isolated vesicles and the
 1509 straight lines represent lines of equal fraction of isolated vesicles. To note that the bomb from
 1510 the UF has the high vesicular core with less than 5% of isolated vesicles, while the three low
 1511 vesicular fragments from the ~~core~~ quenched edge have more than 25% of isolated vesicles
 1512 (see pink spots); d) Darcian viscous permeability (k_1) versus ~~the~~ vesicularity fraction for the
 1513 four typologies of clasts collected at the MV. For comparison, two fluidal fragments and one

1514 | [spiny opaque fragments from](#) ~~Data from June 2014 eruption and~~ February 2015 eruption are
1515 reported.

1516



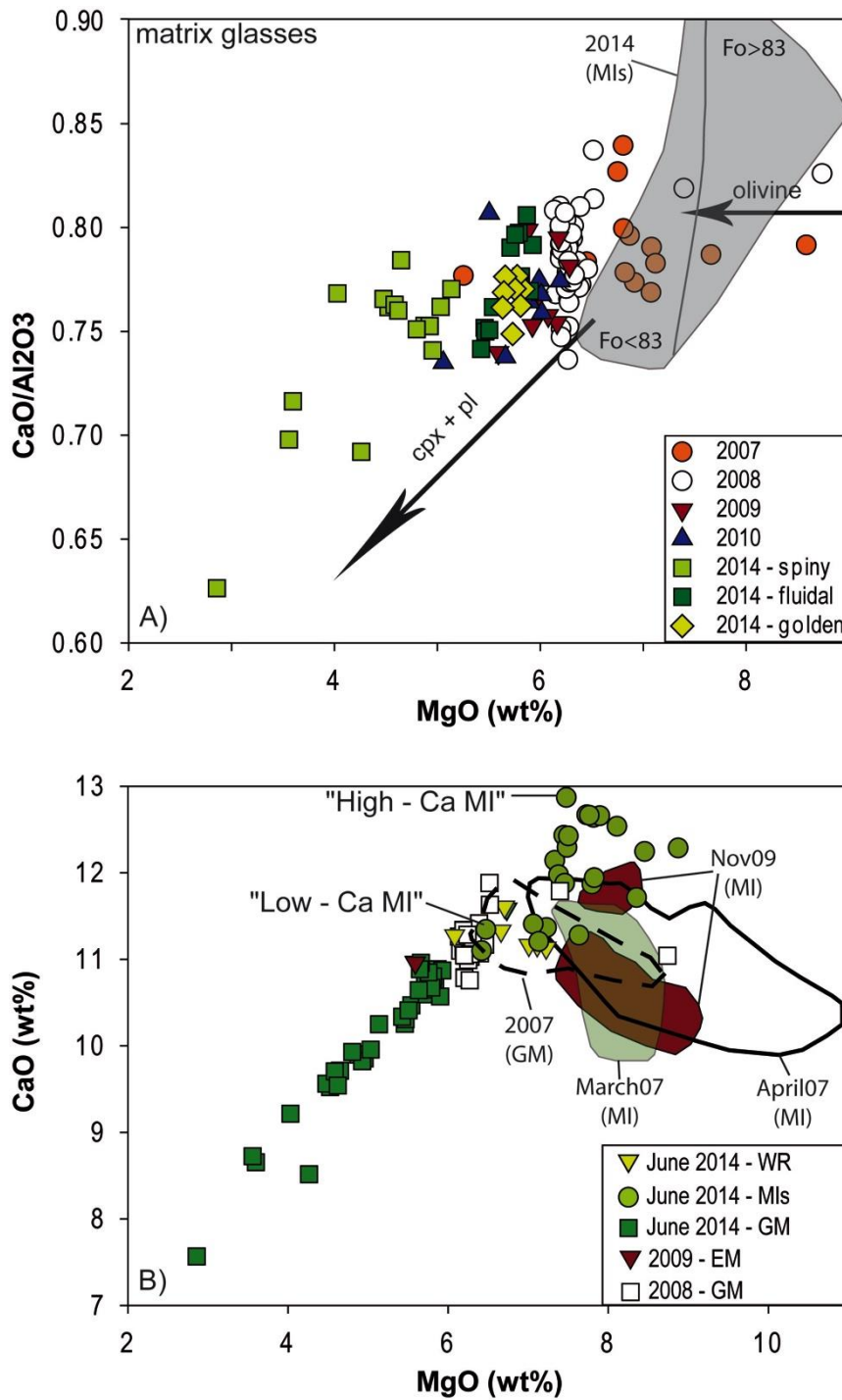
1517

1518 **Figure 7** Ni-Cr concentration plot. (a) Ni-Cr signature of the June 2014 lavas compared to
 1519 that of recent eruptions (Di Muro et al. (2015) and unpublished data). Whole-rock (circles)

1520 and glass (triangles) compositions are shown for the June 2014 eruption. Olivine controlled
1521 lines are indicated for olivine hosting 1.2 and 0.6 wt.% Cr-spinel. Compositions used for
1522 olivine (Ni=1900 ppm, Cr=300ppm), clinopyroxene (Ni=970 ppm, Cr=4800 ppm), and Cr
1523 spinel (Ni=1500 ppm, Cr=25%) are inferred from [Welsch et al. \(2009\)](#), [Salaün et al. \(2010\)](#),
1524 [and Di Muro et al. \(2015\)](#)~~and [Welsch et al. \(2009\)](#)~~. (b) Zoom of the Ni-Cr relationship
1525 between glass (triangles) and whole-rock (circles) samples from the June 2014 eruption.
1526 Fracture I = Western Fracture, Fracture II = Upper Fracture. Careful sample selection has
1527 permitted to obtain a set of virtually olivine-cpx free crystals. Any addition of mafic crystals
1528 translates into enrichment in Ni-Cr; those samples that contain a few % of crystals (consistent
1529 with textural and petrological observation) are slightly enriched in compatible elements.

1530

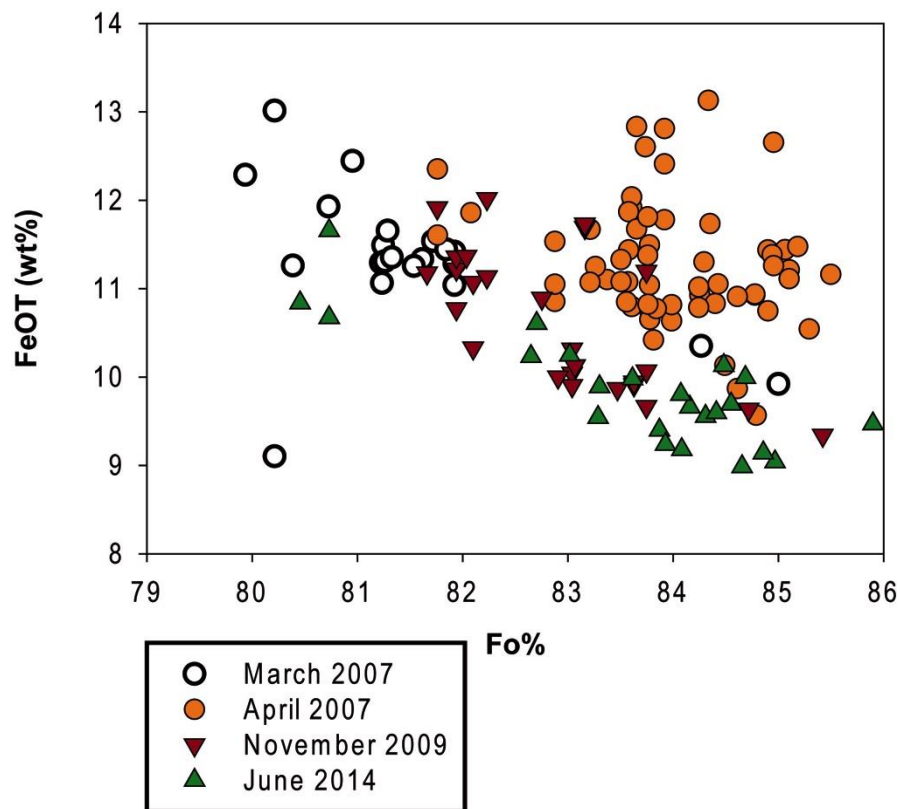
1531



1532

1533 **Fig. 8** (a) Evolution of CaO/Al₂O₃ ratio in the matrix glasses of recent eruptions at Piton de la
 1534 Fournaise as a function of MgO content (directly proportional to melt temperature). MI =
 1535 Melt inclusions (grey area for the 2014 samples). (b) CaO versus MgO content for Piton de la
 1536 Fournaise products. WR = whole rock, GM = ground mass; MI = melt inclusion, EM =
 1537 embayment glass

1538



1539

1540 **Figure 9** FeO_T in melt inclusions as function of Fo content of the olivine host for recent
 1541 eruptions at Piton de la Fournaise

1542

1543

1544

1545

1546

1547

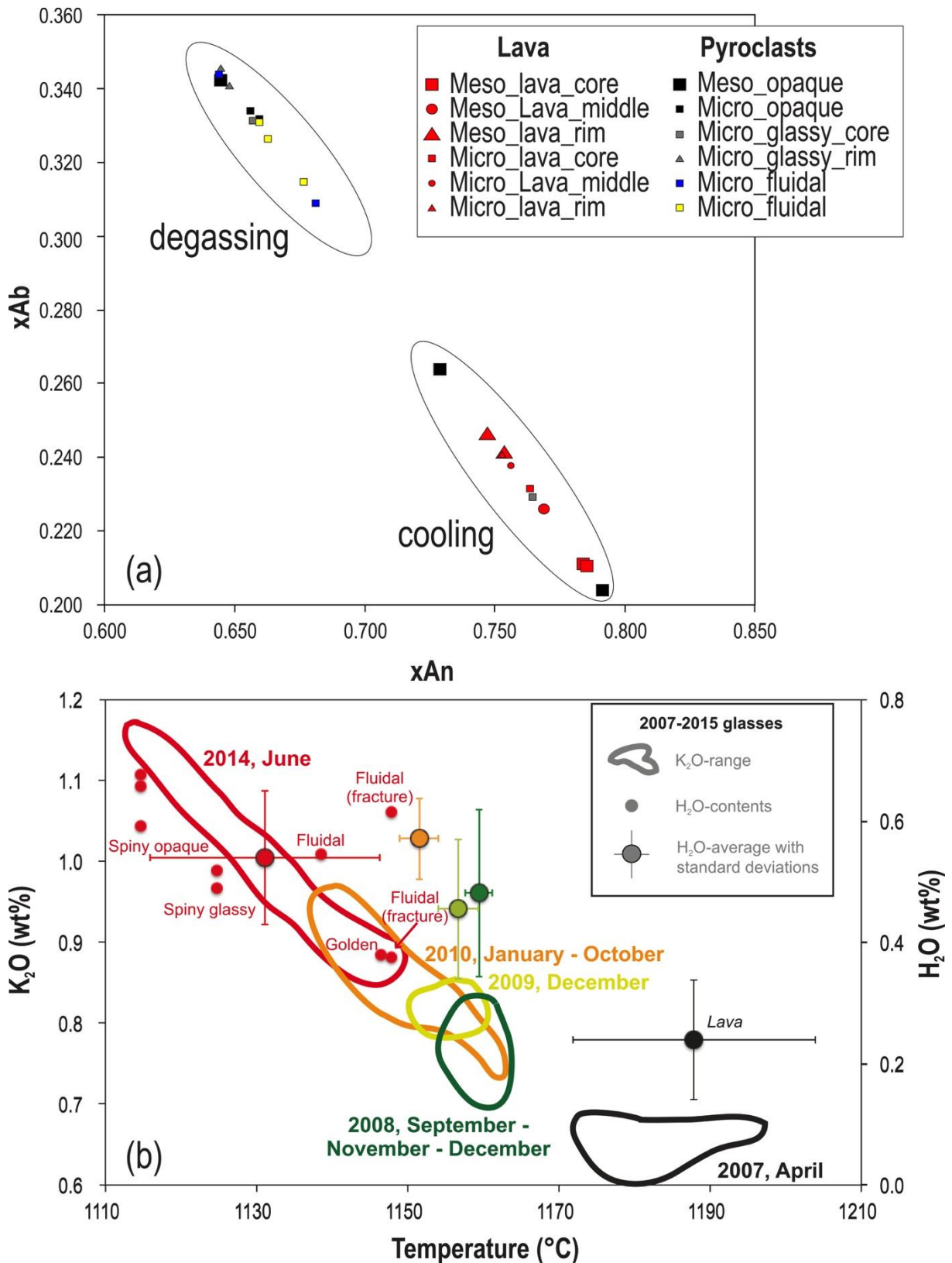
1548

1549

1550

1551

1552



1553

1554 **Figure 10** a) Anorthite versus Albite compositions for the plagioclase crystals measured for
 1555 June 2014 eruption of PdF; b) Temperature, composition (K₂O) and dissolved water content
 1556 (H₂O) for the evolution of 2007-2014 melts from glasses. The data have been obtained by

1557 studying the glass-plagioclase equilibrium or on the basis of matrix glass analyses.
1558 Temperature estimation based on the MgO-thermometer of Helz and Thornber (1987)
1559 | modified by Putirka (2008). Water content is from the plagioclase hygrometer of Lange et al.
1560 (2009). Only plagioclases in equilibrium with melts are considered, following the procedure
1561 described by Putirka (2008) for $>1050^{\circ}\text{C}$ melts ($K_d = 0.27 \pm 0.05$). Error bars reported in
1562 Figure 10b correspond to the standard deviation of the plagioclase dataset, whose range is
1563 | larger than error of the method. We stress that the reported temperatures are obtained using
1564 Helz dry model. F; ~~f~~ further uncertainty arises from the dependence of the method on dissolved
1565 | water content as shown recently by Putirka (2008). I in order to minimize the number of
1566 assumptions and perform a comparison between distinct eruptions, we preferred to adopt the
1567 dry model.

1568

1569

1570

1571

1572

1573

1574

1575

1576

1577

1578

1579

1580

1581

1582

1583

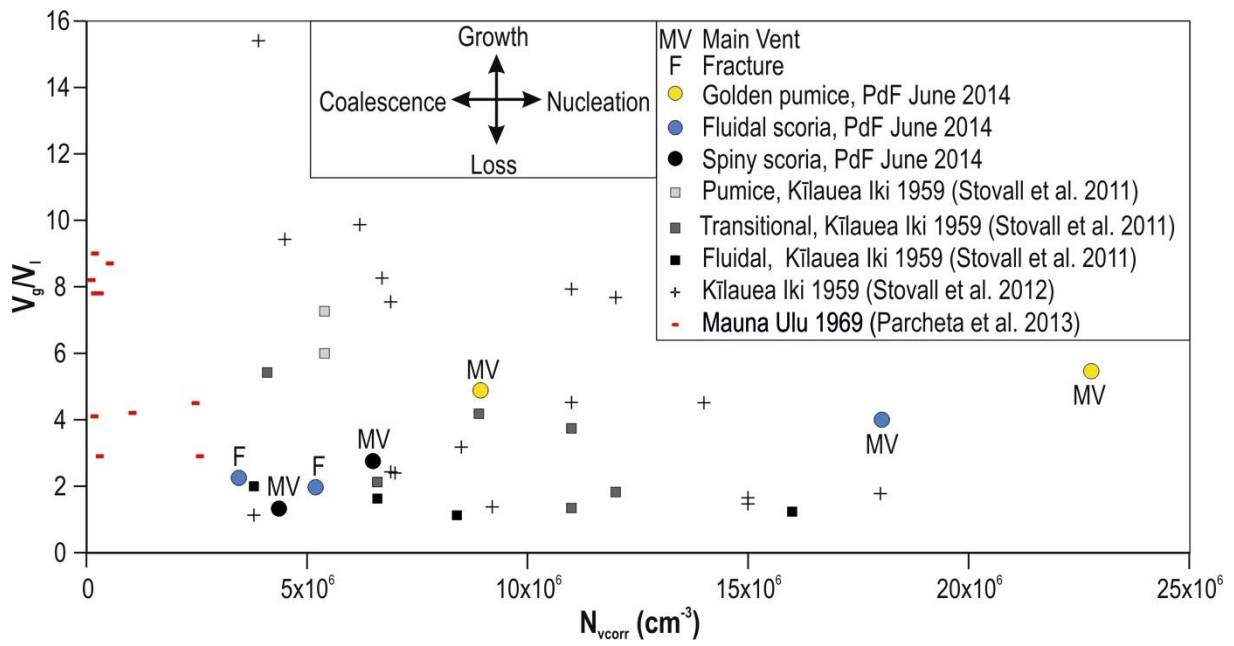
1584

1585

1586

1587

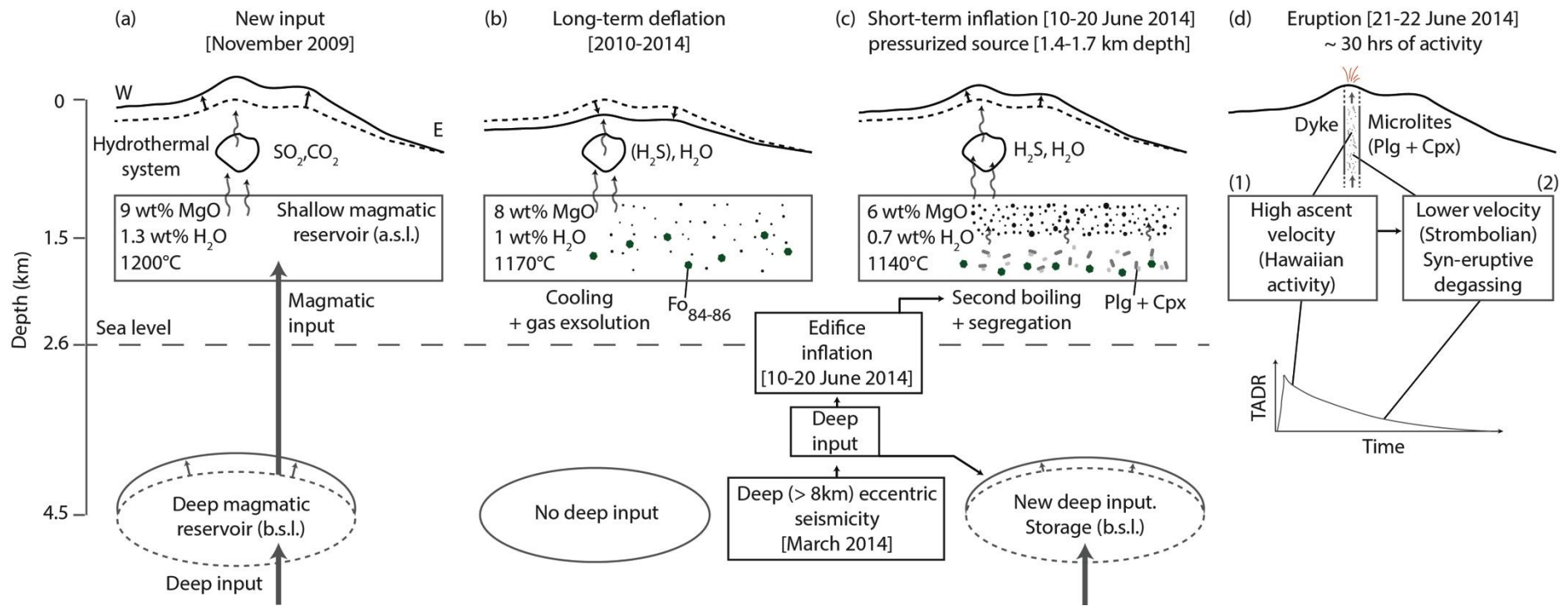
1588



1589

1590 **Figure 11** Volumetric ratio of vesicles to melt (V_G/V_L) versus vesicle number density

1591



1592

1593 **Figure 12** Schematic model of the evolution of PdF volcanic system from the new deep magmatic input of November 2009 up to June 2014

1594 eruption. See explanation in the text



Laboratoire
Magmas &
Volcans



Lucia Gurioli
Physicienne

Laboratoire Magmas et Volcans
Université Clermont Auvergne –
CNRS - IRD, OPGC
Campus Universitaire des Cézeaux
6 Avenue Blaise Pascal
TSA 60026 - CS 60026
63178 AUBIERE Cedex
Tel: +33 (0)473346782
Fax: +33 (0)473346744
l.gurioli@opgc.univ-bpclermont.fr
WEB: <http://www.opgc.univ-bpclermont.fr/>

Date:13/12/2017

Dear Mike,

Please, find the revised version of the paper where we left all the corrections highlighted and the clean version. Figures and Supporting Material are the same.

We are very glad that you appreciated our corrections. We tried to do our best.

We went through your minor corrections carefully and we checked all the text and captions again.

Below you can follow our corrections:

Line 26: I suggest that you change “lightest” to “least dense”. “Light” can also refer to colour. Yes, we changed it everywhere in the text. Very good point.

Line 34: “led”.

Changed

Line 70: “...the spatial and temporal evolution of magma...”

Changed

Line 78: References should be in chronological order.

I made all the references lists in chronological order

Line 108: “endogenic” rather than “intruded”?

Yes, I agree to avoid genetic interpretation

Line 202 and elsewhere: “PdF”, no?

Yes, I changed everywhere

Line 225: “Sampling”.

Corrected

Line 289: Should permeability not be mentioned in the subheading?

Added

Line 312: You should mention that the measurements were performed at atmospheric pressure (i.e. without confining pressure). You should also mention the pore fluid you used and

whether/how you checked for turbulent flow (the Forchheimer effect). Please provide more details here.

I added more details. Could you check it please? Line 283

Line 315: Do not abbreviate the names of the minerals.

Yes, corrected everywhere

Line 458 and elsewhere: “Light” can also refer to colour. “Low-density” is a better descriptor, in my opinion.

We completely agree

Line 504: “Clusters”.

Corrected

Line 506: Rephrase to avoid “picture”.

We rephrased it

Line 524: “percent”, not “percentage”.

Corrected

Lines 527 and elsewhere: Are you referring here to a percentage or percentage points? If you’re talking about percentage points, perhaps it’s best to stick with “30 vol.%”.

Yes, corrected everywhere in vol. %

Line 530: This is the results section. Since you now show values of permeability, there should be at least a couple of sentences describing the data.

I added more details. Could you check it please? Line 486

Line 668: Remove comma.

OK

Line 727: “experienced”. In fact, please reword this sentence to improve clarity.

I reword it

Line 806: Please reword the sentence starting “The proportion...”

I reword it

Line 852 and elsewhere: Do not abbreviate the names of the minerals.

Corrected everywhere

Line 853: “indicates”.

OK

Line 889: References for the published expansion signatures?

I reword it because the references are reported earlier and we wanted to refer to the evidence of the expansion in the graph of figure 11; see line 838

Line 916: Remove comma.

OK

Line 924: “and”.

OK

Line 926: Impermeable means that fluid cannot pass. Please rephrase this sentence to use “low-permeability”.

I reword it

Line 948: “pathway”.

OK

Line 948: Do the authors mean “very low permeability” or “impermeable” here?

Actually the authors speak about a unmeasurable permeability and Amanda in her paper reports “impermeable samples” in Fig 1 (Lindoo et al; 2017). However, I added “almost” impermeable

Line 1041: “feeds”.

OK

Line 1044: “crystals”.

OK

Line 1053: Should this one-sentence paragraph not be part of the previous paragraph?

Yes, we added to the previous paragraph

Line 1217: Due to the number of changes, it's difficult to follow the conclusions. The authors should make sure there are no typos/grammatical errors.

As I said, I read it carefully, my first two co-authors did the same, but no-one of us is English. We hope that we found all the errors, or at least all the inconsistency; see other corrections that we added

Figure 5: The figure still contains the Morphology G3 results. I suggest that the authors double-check all the figures and figure captions.

I fixed it

Sincerely

Lucia and co-authors